ARMY RESEARCH LABORATORY

An Atmospheric Turbulence Profile Model for Use in Army Wargaming Applications I

by David H. Tofsted, Sean G. O'Brien, and Gail T. Vaucher

ERRATA SHEET

re: ARL-TR-3748, *An Atmospheric Turbulence Profile Model
for Use in Army Wargaming Applications I*, **February 2006,
by David H. Tofsted, Sean G. O'Brien, and Gail T. Vaucher**

This is an errata sheet for ARL-TR-3748. Please insert this sheet immediately after the cover page of the original document.
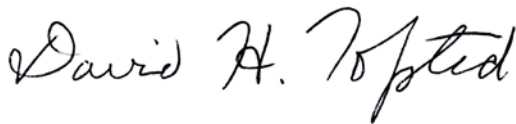
Page
39

Equation (48) reads:

$$C_{TS}^2(z) = C_T^2(z_r) \frac{z^{-2/3}\left[1 - 7\left(z/L_{Ob}\right)\right]^{-2/3}}{z^{-2/3}\left[1 - 7\left(z_r/L_{Ob}\right)\right]^{-2/3}} . \tag{48}$$

Equation (48) should read:

$$C_{TS}^2(z) = C_T^2(z_r) \frac{z^{-2/3}\left[1 + 2.4\left(z/L_{Ob}\right)^{+2/3}\right]}{z_r^{-2/3}\left[1 + 2.4\left(z_r/L_{Ob}\right)^{+2/3}\right]} . \tag{48}$$

A corrected PDF version of this report will be available in the ARL Technical Reports section on the ARL Web site under February 2006:

http://www.arl.army.mil/www/default.cfm?Action=17&Page=239&Topic=TechnicalReports&Year=2006

David H. Tofsted

U.S. Army Research Laboratory
Computational and Information Sciences Directorate
RDRL-CIE-D
White Sands Missile Range, NM 88002-5501

NOTICES

Disclaimers

The findings in this report are not to be construed as an official Department of the Army position unless so designated by other authorized documents.

Citation of manufacturer's or trade names does not constitute an official endorsement or approval of the use thereof.

DESTRUCTION NOTICE—For classified documents, follow the procedures in DoD 5220.22-M, National Industrial Security Program Operating Manual, Chapter 5, Section 7, or DoD 5200.1-R, Information Security Program Regulation, C6.7. For unclassified, limited documents, destroy by any method that will prevent disclosure of contents or reconstruction of the document.

Army Research Laboratory

White Sands Missile Range, NM 88002-5501

An Atmospheric Turbulence Profile Model
for Use in Army Wargaming Applications I

David H. Tofsted, Sean G. O'Brien, and Gail T. Vaucher
Computational and Information Sciences Directorate
Battlefield Environment Division

REPORT DOCUMENTATION PAGE

Public reporting burden for this collection of information is estimated to average 1 hour per response, including the time for reviewing instructions, searching existing data sources, gathering and maintaining the data needed, and completing and reviewing the collection information. Send comments regarding this burden estimate or any other aspect of this collection of information, including suggestions for reducing the burden, to Department of Defense, Washington Headquarters Services, Directorate for Information Operations and Reports (0704-0188), 1215 Jefferson Davis Highway, Suite 1204, Arlington, VA 22202-4302. Respondents should be aware that notwithstanding any other provision of law, no person shall be subject to any penalty for failing to comply with a collection of information if it does not display a currently valid OMB control number.
PLEASE DO NOT RETURN YOUR FORM TO THE ABOVE ADDRESS.

1. REPORT DATE *(DD-MM-YYYY)*	2. REPORT TYPE	3. DATES COVERED (From - To)
February 2006	Final	August 2004 – September 2005

4. TITLE AND SUBTITLE	5a. CONTRACT NUMBER
An Atmospheric Turbulence Profile Model for Use in Army Wargaming Applications I	
	5b. GRANT NUMBER
	5c. PROGRAM ELEMENT NUMBER

6. AUTHOR(S)	5d. PROJECT NUMBER
David H. Tofsted	
Sean G. O'Brien	5e. TASK NUMBER
Gail Tirrell Vaucher	
	5f. WORK UNIT NUMBER

7. PERFORMING ORGANIZATION NAME(S) AND ADDRESS(ES)	8. PERFORMING ORGANIZATION REPORT NUMBER
U.S. Army Research Laboratory Computational and Information Sciences Directorate Battlefield Environment Division (ATTN: AMSRD-ARL-CI-EE) White Sands Missile Range, NM 88002-5501	ARL-TR-3748

9. SPONSORING/MONITORING AGENCY NAME(S) AND ADDRESS(ES)	10. SPONSOR/MONITOR'S ACRONYM(S)
U.S. Army Research Laboratory 2800 Powder Mill Road Adelphi, MD 20783-1145	
	11. SPONSOR/MONITOR'S REPORT NUMBER(S)

12. DISTRIBUTION/AVAILABILITY STATEMENT

Approved for public release; distribution is unlimited.

13. SUPPLEMENTARY NOTES

14. ABSTRACT

Models for the vertical structure of the refractive index structure parameter, C_n^2, appropriate for wargames are discussed. Legacy vertical profile models are reviewed and synthesized to produce a new vertical model that seamlessly spans various segments of the tropospheric atmosphere. The model integrates effects for the surface, boundary, and upper tropospheric layers. Legacy models are reviewed and synthesized to create the new profile model. In this effort the focus has been on the worst case condition near the surface of daytime noon turbulence. The model developed is suitable to simulate turbulence effects on Army electro-optical sensors for visible through far-infrared wavelengths. The products of this study is a tailored, small, rapidly executing algorithm and associated tables for predicting turbulence: a log-mean vertical layer and terrain effects prediction, and a methodology for conversion of the log-mean profile to mean C_n^2 profile.

15. SUBJECT TERMS

Similarity Theory, Troposphere, Boundary Layer, Surface Layer, Wargaming, Optical Turbulence, Refractive Index Structure Parameter

16. SECURITY CLASSIFICATION OF:			17. LIMITATION OF ABSTRACT	18. NUMBER OF PAGES	19a. NAME OF RESPONSIBLE PERSON
a. REPORT	b. ABSTRACT	c. THIS PAGE	SAR	60	David Tofsted
U	U	U			19b. TELEPHONE NUMBER *(Include area code)* 505-678-3039

Contents

List of Figures

List of Tables

Executive Summary

In recent years several new surveillance technologies have been developed to improve standoff range at which enemy personnel, activity, and equipment can be detected, identified, and engaged. Different wavelengths are being explored for these new Army electro-optical sensors. Most of these sensors operate at shorter wavelengths than traditional far-infrared imaging devices developed during the 1970's and 1980's. As a result, the influence of optical turbulence on these systems is significantly greater, requiring that turbulence effects be directly included in wargaming simulations of sensor performance. The key parameter governing optical turbulence effects is the refractive index structure parameter C_n^2.

This parameter is a highly variable function of location in the earth's atmosphere. It also varies extremely over the course of a day even at a single location. Near the earth's surface, it can vary by four orders of magnitude. It also can vary by several orders of magnitude with height above a single point. To determine the effects of C_n^2 on a given system, one must integrate the C_n^2 value over a path between sensor and target. Usually this path integral is weighted according to some dimensionless function of path position. The specific effect will also depend on wavelength, receiver aperture diameter, path length, and possibly the inner scale of turbulence. For now, we are less concerned with inner scale, which perturbs the general results, than we are with the overall strength of turbulence, C_n^2. The basic problem is to posit a model of this parameter as a function of time and height above the surface. In this document we mainly focus on height functionality.

Several models of C_n^2 variation with height have been previously developed. Unfortunately, most of these models only consider limited altitude ranges. For example, the Air Force developed the Air Force's Maui Optical Station (AMOS) and Critical Laser Enhancing Atmospheric Research (CLEAR) models applicable to conditions above their Mauna Loa summit observatory and the southern New Mexico desert, respectively. A more general model with wide application is the Hufnagel-Valley model. Unfortunately, this function of height model is mainly useful for nighttime earth-to-space applications. It performs particularly poorly during daytime conditions where turbulence is the strongest near the surface, which is the time of day that is most stressing to performance of Army systems.

To provide a single model suitable for simulation of vertical structure conditions it was decided that these disparate models covering different portions of the atmosphere (surface layer, boundary layer, upper troposphere) could be blended together into a single model. The distinguishing feature of the model developed is the coupling of the different models of height dependence in different altitude regions of the atmosphere into a single height model.

We then discuss the governing parameters of this profile model. The primary parameters are the height of the elevated inversion layer and the turbulence strength at a standard height. We analyze historical boundary layer height data to develop a function of height of the inversion layer versus time of day for different months of the year. This function is then used to derive one of the main governing atmospheric structure parameters, which can be computed directly based on time of day, month, and sky cover. Follow-on work will extend this picture to cover the temporal structure of the turbulence depending on time of day, climate, local terrain, and current weather conditions. Like some previous models of diurnal evolution, such as HELHEM, this model was tailored primarily for the southern New Mexico area and may require modification for more general applications.

The vertical structure model then consists of equations combining effects of each layer combined into a total form in the following equation[1]:

$$C_n^2(z) = 10^{N(z) + \sigma^2(z)/2}.$$

Inputs to the model include the time of day and month of year, cloud cover fraction, and surface meteorological measurements of wind speed, temperature, and an estimate of the current C_n^2 strength. Since this last value is not normally available, we intend to extend the HELHEM model to provide an estimate of C_n^2 based on local weather, terrain, and time of day conditions.

The preceding equation also requires information concerning the log-normal distribution of turbulence strength. This is because log-mean C_n^2 is not the same as the average C_n^2. The two are related through the form of the log-normal distribution. The variance of this distribution is required to determine the mean C_n^2 based on log-mean statistics that arise from models such as CLEAR and AMOS.

We conclude with the result that our efforts have produced a tailored, small, rapidly executing algorithm and associated tables for predicting turbulence: a log-mean vertical layer prediction, and a methodology for conversion of log-mean statistics to a mean C_n^2 profile required for assessing turbulence effects on simulated sensors in wargames. Further efforts will focus on temporal evolution of the turbulence strength and the influences of weather and terrain.

---

[1] This is equation 47 that can be found on page 37 in the report.

1. Introduction

For many Army systems a primary goal is to increase the standoff range at which the enemy may be detected, identified, and engaged. Army electro-optical systems are continually being improved to increase their range and performance. However, as engagement range increases, effects of optical turbulence also increase. In general greater turbulence effects are experienced by shorter wavelength systems as well. Nonetheless, due to their greater resolution, shorter wavelength systems are being considered for Army use. Therefore, for proper comparison purposes it seems reasonable to factor in the effects of turbulence to predictions of system performance in future Army wargaming models.

The most basic quantity characterizing the strength of atmospheric turbulence is the refractive index structure parameter, C_n^2. The main source of this turbulent energy is the mixing of air masses of different densities. Such mixing is primarily driven by surface heating and cooling. At higher altitudes it is also driven by the mixing of air masses of different density due to wind shear, vertical convective motions, and/or wave action. To characterize the effects of turbulence in any given situation usually depends on evaluating a parameter of interest along a specific line-of-sight (LOS). The C_n^2 parameter is ubiquitous in its presence in these various integrals. Integrals are available to characterize turbulence effects on such propagation effects as image blur, apparent motion, laser beam divergence, scintillation, and beam wander. C_n^2 is sometimes referred to as the refractive index structure *constant*, but it is far from constant. Rather, C_n^2 fluctuates by orders of magnitude over the course of a single day at heights close to the surface. This region is called the surface layer, consisting of the first 20–200 m of atmosphere above the earth's surface. Besides being a function of time, C_n^2 is also a function of height and horizontal position. C_n^2 drops in value rapidly as a function of height during the day. This means that the amount of turbulence encountered depends critically on the height of the LOS above the terrain and thus requires individual calculations for each unique target-to-observer geometry. We will discuss these LOS integrals again in section 1.1.

Of more direct concern in this report is the means of evaluating the vertical structure of C_n^2 itself. Because of varied production mechanisms, the structure of turbulence changes character with height above the ground. To model the vertical variations of C_n^2 we thus have to account for these different mechanisms through representative profiles of C_n^2 that change in form with height. Nevertheless, the model proposed is rather simplified since we do not attempt to correlate such profiles to other atmospheric forcing parameters. For instance, we do not consider the stratospheric inversion at the top of the troposphere, the influence of the jet stream, gravity waves, turbulent plumes, cloud cover, the elevated inversion during the day, the structure of the surface based inversion at night, or surface visibility, though each of these has an influence on

1

the value of the C_n^2 at the ground, its vertical structure aloft, and its evolution with time. For such a complete model, considerable additional research would be necessary.

For our purposes we propose to provide not a complete physical model, but rather a profile which is characteristic of the vertical structure. In this sense, we hope to provide a seamless profiling method that ranges from the earth's surface up to the top of the troposphere. While not perfect, it should provide sufficient fidelity to be useful under a variety of atmospheric conditions. The height domain chosen for these models supports characterization of turbulence effects for the complete range of Army systems that may appear in Army simulations. Many Army systems operate within the first few meters above the earth's surface. These include the full assortment of light and heavy Army forces. Helicopters operate further from the surface, but within the boundary layer atmosphere which can extend up to 2–3 km above ground level (AGL). Unmanned Aerial Vehicles (UAVs) operate up to thousands of feet above the surface, but still within the troposphere. Vertical profiles of C_n^2 must therefore be available to characterize these various regimes in a seamless manner, starting at the ground and continuing into the upper troposphere. While various standard profiles exist (see Beland, 1993, for an extensive discussion) most existing models represent a patchwork of vertical structures covering various sections of the vertical regime, but none currently seem to address the profile as a whole. An exception to this observation appears to be the Hufnagel-Valley (H-V) model, which we will discuss. However, there are certain significant concerns regarding the validity of this model as it applies to the boundary layer atmosphere. As a consequence, we will consider a new model of the vertical structure of turbulence.

The first step in this development is to examine various legacy turbulence profile models. We then extract features from several of these to synthesize a single new model which is capable of simulating a complete vertical profile of the troposphere. The proposed profile model includes features that adjust for arbitrary surface measured turbulence levels and stability. The model is thus compatible with surface layer dynamic similarity theory (Wyngaard, 1973). This surface layer model is then integrated into a daytime boundary layer model first proposed by Kaimal et al. (1976). However, a nighttime version of the Kaimal model was never proposed. We use similarity model surface layer behavior to infer vertical structure beyond the surface layer that is consistent with the Air Force's Maui Opitical Station (AMOS) profile model (Beland et al., 1988) used to characterize the AMOS and Critical Laser Enhancing Atmospheric Research I (CLEAR I) night models, as reported by Beland (1993). This links the boundary layer interface to the upper troposphere. The CLEAR I profile was based on measurements made in the Tularosa Basin area of southern New Mexico (Garvey et al., 1985), part of the high altitude Chihuahuan desert. As a point of reference, models appropriate for this area should also be typical of other mid-latitude desert regions.

We also discuss perturbations in C_n^2 about the log-10-mean values given by the vertical profile model. The rationale here is that the LOS integrals of turbulence effects involve the actual values of C_n^2 along the path, while the available models only provide a log-10-mean C_n^2 value.

As will be shown, when considering a log-normally distributed variable, first the variance of the distribution in the log space affects the calculation of the mean in the scalar space. Secondly, when considering a single LOS, temporally varying C_n^2 can cause fluctuations in acquisition performance due to variability in the clarity of an observed target image. These variations may affect the pace of a simulated battle or differentiate the performance of otherwise identically functioning systems. The statistics of C_n^2 temporal variability are thus necessary. We will discuss these temporal variations for surface-to-surface situations only.

1.1 Parameters of Interest

As illustrations of how C_n^2 is employed we consider two parameters often used to characterize turbulence effects on systems: the turbulent coherence length, ρ_0 [m], and the isoplanatic patch size, θ_0 [mrad]. These two parameters are closely related. The first is used in studying blur effects on receiver systems. The second is used in astronomical applications to determine an angular distance at which two moving points appear to shift position in unison. Outside the angle θ_0 two stars, for example, will appear to move as separately moving points of light. It is said that the wavefront from two such apparently separately moving objects has become *anisoplanatic*.

We evaluate these parameters via integrals over the optical path starting at $z = 0$ at the receiver end of the path, to $z = L$ at the object end of the path, and we assume (for now) the turbulence spectrum has a Kolmogorov form (zero inner scale, infinite outer scale). The two parameters ρ_0 and θ_0 are written in integral form as (Beland, 1993, equation 2.135),

$$\rho_0 = \left[1.46\, k^2\, \sec(\varphi) \int_0^L C_n^2 \left(1 - s/L\right)^{5/3} ds \right]^{-3/5}, \tag{1}$$

where $C_n^2(s)$ is the turbulence as a function of path position s [m], L is again the path length [m], and $k = 2\pi / \lambda$ is the radiation wavenumber [m^{-1}] is the radiation wavelength [m]), and (Beland, 1993, equation 2.170),

$$\theta_0 = \left[2.91\, k^2\, \sec^{8/3}(\varphi) \int_0^L C_n^2(s)\ s^{5/3}\ ds \right]^{-3/5}, \tag{2}$$

where φ is the zenith angle of the observation direction from the observer to the target. Most astronomical applications take $\varphi = 0$ to represent a vertical path. Thereby $\sec(\varphi) = 1$. If it is further assumed that the object of interest (target) is above the top of the atmosphere, then ρ_0 simplifies to an evaluation of

$$\rho_0 = \left[1.46\, k^2\, \sec(\varphi) \int_0^{L_T} C_n^2\ ds \right]^{-3/5}, \tag{3}$$

where L_T is the range to the top of the atmosphere as opposed to the range to the target itself. θ_0 similarly reduces to,

3

$$\theta_0 = \left[2.91 \; k^2 \; \sec^{8/3}(\varphi) \int_0^{L_T} C_n^2(s) \; s^{5/3} \; ds \right]^{-3/5}. \tag{4}$$

Because of the different weighting functions involved, ρ_0 will tend to be affected by the turbulence closest to it, while θ_0 will be either most affected by turbulence weighted toward the top of the atmosphere (astronomical case) or toward the target. On the other hand, systems affected most by scintillation (active sensors) will be most affected by turbulence near the center of the path. Hence, evaluations of turbulence impacts depend on effects at different points along the path for different sensors. Path integrations are thus crucial to determining the specific turbulence effects on individual sensors. But for the specific case of passive imaging sensors we can characterize most of the turbulence effects using the single parameter of ρ_0, the coherence length. We consider this issue in detail in section 8.

1.2 The Hufnagel-Valley Profile

As an example of a vertical profile model, we consider the H-V model. This model (Beland, 1993), consists of an amalgamation of the original Hufnagel (1974) model, and its extension to the ground by Ulrich (1988), based on a suggestion by Valley (1980). We choose this model to begin our investigations because it is very well known and often cited (Beland, 1993; Roggemann and Welsh, 1996; Andrews and Phillips, 1998; Andrews et al., 2001). Two reasons appear to explain the popularity of this model. First, it is rather simple. Featuring only two parameters to manipulate, the H-V model can be described using only a surface level value of C_n^2 [$C_n^2(0)$], and an upper level wind speed, U, given as the Root Mean Square (rms) windspeed [m/s] averaged over the 5–20 km AGL range. The H-V model has a very simple form:

$$C_n^2(z) = 8.148 \times 10^{-26} \; U^2 \; Z^{10} \; \exp(-Z) + 2.700 \times 10^{-16} \; \exp(-Z/1.5) + C_n^2(0) \exp(-10Z). \tag{5}$$

with Z the height AGL in kilometers.

Second, the H-V model features a standard implementation, the so-called H-V 5/7 model, for which integrated ρ_0 and θ_0 yield the *typical* $\rho_0 = 5$ cm and $\theta_0 = 7 \; \mu$ rad values commonly assumed for nighttime conditions in the field of astronomy (hence, the 5/7). These results, assuming a vertical path integration, and propagation wavelength $\lambda = 0.5 \; \mu$ m, $C_n^2(0) = 1.7 \times 10^{-14}$ m$^{-2/3}$, and U=21m/s. For many nighttime astronomical observation conditions, these results are indeed typical. But the H-V model is less well equipped to treat other times of the day. Particularly for daytime conditions a better model must be sought. The Kaimal model's consideration of the boundary layer inversion's impact on C_n^2 appears better suited to describing the daytime elevated inversion. This model predicts a turbulence increase at the base of the elevated inversion layer. The daytime atmosphere will also feature extremes of turbulence in the surface layer immediately next to the ground. Wyngaard (1973) indicates vertical structures of turbulence should be scaled according to the Monin-Obukhov length (L_{Ob}) in the surface layer through the dimensionless ratio z/L_{Ob}, where z is height above the surface [m]. Further from

the surface $(z > L_{Ob})$, the daytime vertical C_n^2 decreases via a $z^{-4/3}$ power law. Under neutral conditions Wyngaard indicates a $z^{-2/3}$ power law and a z^0 law for stable (nighttime) conditions. Comparing these rules for the so-called free convection region of the boundary layer (approximately 100–1000 m AGL) one finds that the H-V model's lead term $A \exp(-z/100)$ does not match well against either the daytime or nighttime profile conditions of Wyngaard. Particularly, the predicted z^0 nighttime behavior does not match the H-V model at all, while the daytime $z^{-4/3}$ behavior can only be matched to the H-V model behavior at a single height, through

$$A \exp(-z/100) = B\, z^{-4/3}; \quad -(A/100)\exp(-z/100) = -(4/3)\, B\, z^{-7/3}. \quad (6)$$

The match height is z=133 m AGL. Below this height the daytime atmosphere has greater C_n^2 and higher gradients. A similar result is obtained under neutral conditions, except that the matching height is z = 67 m AGL. In either case, the lack of a correspondence to existing surface layer behavior indicates the H-V model is not well adapted for near ground-level applications.

2. General Profile Characteristics

In this section we consider more carefully the nature of vertical structure profiles of the log-mean C_n^2. As illustrated by the H-V profile, smoothly varying functions of C_n^2 variability with altitude in the upper troposphere are available. In fact, much work was done in the early-to-mid-1980's. The emphasis in that era was largely on earth-to-space applications. Our focus is somewhat more limited, yet still considers most of the troposphere where a majority of the turbulent influences arise. We begin with the first few kilometers of the lower troposphere, a region termed the boundary layer or sometimes called the planetary boundary layer. During the day, the upper boundary of this layer usually consists of an elevated capping inversion. Part of the effect of this cap is to keep a layer of aerosols trapped underneath this inversion level. Air heated at the surface tends to move vertically through the boundary layer, often augmented in its transport vertically by turbulent plumes powered by intense surface heating which causes a very steep temperature lapse rate in the lower few hundred feet of the atmosphere. These plumes, if they are strong enough, can sweep up dust, sand, and debris from the surface in desert regions, becoming visible as dust devils. The boundary layer thus tends to select efficient means of transporting of heat through the layer, depositing this heat into the capping inversion rather than heating the air between. Nevertheless, due to entrainment and air recirculation, over time the boundary layer becomes mixed. Adjacent to the surface, a layer develops which may be characterized by dynamic similarity theory (Haugen, 1973). The properties of this layer are dominated by drag effects of the ground. Their chief scaling parameter is distance from the

surface, z, and scaling length L_{Ob}. This length scales the height dependence of nearly every mean parameter (wind speed, temperature, humidity, etc.), including C_n^2.

The nature of this surface layer is such that a predawn surface based inversion (region 1 of figure 1) is replaced by a superadiabatic lapse condition (negative vertical potential temperature gradients up to the base of the entrainment zone) (region 2 in figure 1). The ambient temperature reaches a local minimum at this height (Z_i [km]) which also marks the base of an elevated inversion layer. As surface heating continues throughout the day, the level of the inversion base rises, reaching a maximum at the time of the evening neutral event (region 3 of figure 1). Such an event marks a time of minimum turbulent activity within the boundary layer. The layer becomes adiabatic (constant potential temperature with height). However, as denoted by region 3 in figure 1, this event may occur at different times within the layer since the upper levels of the layer may still contain residual fluctuations of temperature even after the surface has become stable. At the ground, the atmosphere then develops a new surface based inversion (region 4 of figure 1), which builds in depth throughout the night. But unlike the daytime atmosphere which reaches a maximum height around mid afternoon, the nocturnal stable layer continues to increase in height through the evening. Partly this is due to the energy fluxes controlling the layer development and partly due to the wind speed evolution which is often driven by the nocturnal low level jet phenomenon which has a time scale longer (on the order of 17 hours) than a typical stable period. Note that in figure 1 height is not to scale.
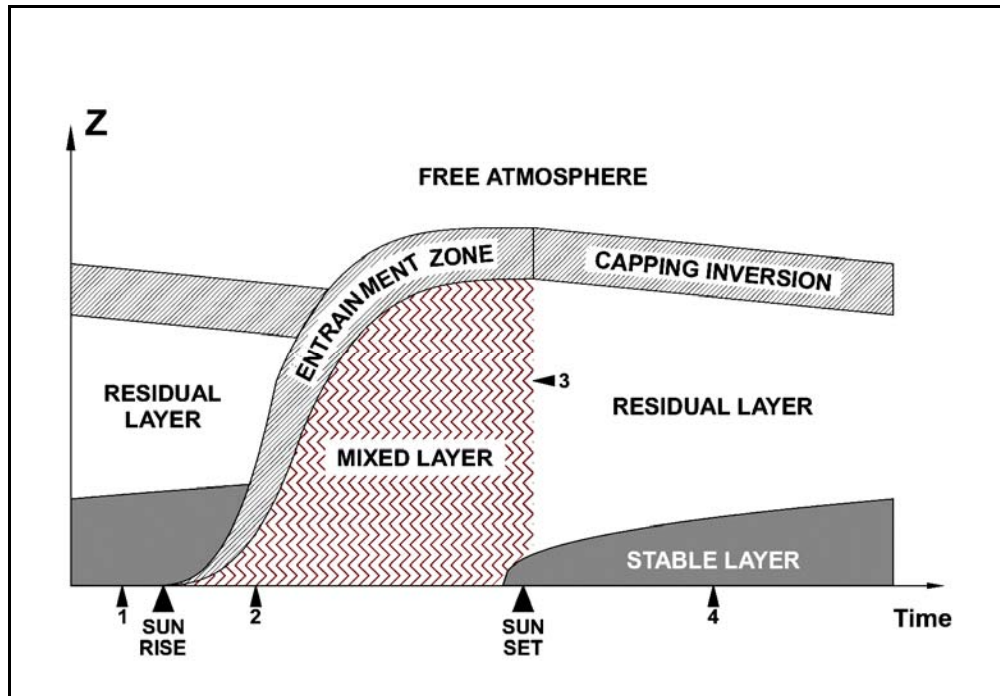

Figure 1. Canonical development of the boundary layer over a diurnal period.

The structure of turbulence within the daytime boundary layer involves a general decrease in C_n^2 with height for the first several hundreds of meters. However, due to the mixing of warm and colder air masses near the inversion layer, there is a turbulence increase near the elevated inversion. Likewise, at night, turbulence near the surface decreases with height, though not as strongly as during the day. Because of gravity wave activity within the boundary layer, which behaves somewhat like a waveguide, the motions of waves and propagating energy are confined to the surface layer, and the fluctuations of temperature within the boundary layer are modeled as roughly constant with height starting at the surface layer. The vertical mixing that occurs within the inversion layers (day or night) tends to both increase the depth of the boundary layer atmosphere as well as cause increased turbulence in the vicinity of the inversion (again day or night). Once above the inversion the atmosphere is approximately neutral, or adiabatic (constant average potential temperature θ with height), up to the level of the tropopause where the effects of the stratospheric inversion layer are felt. Within this neutral layer, the turbulence level drops with increasing altitude due to declining pressure and temperature levels (as discussed in section 4.2). At the base of the stratospheric capping inversion, models such as H-V, CLEAR I, and AMOS all agree that the profile should exhibit increased turbulence (a {\it bump}). For the H-V profile this bump appears as the first term in the expression in equation 5. In this case the bump appears around 11 km. The CLEAR I and AMOS models, discussed in section 6, exhibit analogous increases around 15 km.

3. Log-Normal Distributions

Having discussed the general vertical properties of the tropospheric atmosphere, we also consider the nature of statistical fluctuations of turbulence along any particular LOS. For horizontal near-surface LOSs these statistics impact the temporal variability of intervisibility along a given line. For LOSs involving UAVs looking downward to objects near the ground, an LOS will pass through a number of statistically independent layers of different C_n^2 value. However, because the C_n^2 statistics above the surface layer are generally horizontally homogeneous, they will not vary significantly with time or position as long as the observation altitude does not vary. Hence, we must treat these two cases as separate but related problems, involving the same statistical properties of the turbulence.

In the first case, we consider temporal variations in the amount of turbulence along a single path. The performance of a specific acquisition task may thus produce varied results, depending on the strength of turbulence currently present along the LOS. Since the turbulence level will tend to fluctuate by up to $\pm 1/3^{\text{rd}}$ of an order of magnitude, the effect of the variation of turbulence will vary the size of the coherence length by a scale factor ranging from 1.0 to 2.5. The time scale of these variations appears to be on the order of 10's of seconds. The effect these fluctuations will have depends on the ratio of ρ_0 to the system entrance aperture diameter, D. The knee of the

atmospheric modulation transfer function (MTF) curve is located around $\gamma = D/\rho_0 = 6$ or $\gamma = D/r_0 \approx 3$ (where r_0 is the Fried coherence diameter ($r_0 = 2.1\,\rho_0$)). For $\gamma > 6$ the system will be significantly affected by the turbulence. For $\gamma < 6$ the turbulence impact will be marginal. For variations of ρ_0 with $\gamma > 6$, the impact of temporal fluctuations in C_n^2 will cause significant temporal variations in performance. Since $\rho_0 \propto L^{-3/5}$, there will always be some range of significance where these effects will be pronounced, however, it may be beyond the effective range of the system in question. On the other hand, for given range (L) and wavelength (λ), there will also always be an equivalent C_n^2 value where these effects become significant.

To model LOS turbulence intensity variations we must know both the probability density function (e.g., Stark and Woods, 1986) for C_n^2 and have some knowledge of the autocorrelation to determine when to make a new independent random draw on the C_n^2 distribution. To first order the distribution of C_n^2 near the ground appears to be log-normal. In log space, therefore, C_n^2 may be characterized by a mean and a standard deviation. An example of this behavior is illustrated in figure 2. The data plotted represent measured C_n^2 fluctuations over a 950 m path that was approximately 4 m AGL. Data were tabulated over a period of approximately two hours to produce the distribution. Over that time the C_n^2 mean value was roughly constant. The raw data were then transformed into a probability density function in log-10 space. Probability data were plotted in increments of 0.01 in log-10-space. The data were collected on June 21, 2001, at the "Tank Tower" located approximately 5 miles east of the headquarters area of White Sands Missile Range (WSMR), NM. The data plotted in figure 2 with computed log-mean C_n^2 of -13.3186, were modeled using a log-normal distribution of C_n^2 with log-mean of -13.295 and log-standard deviation of 0.215.
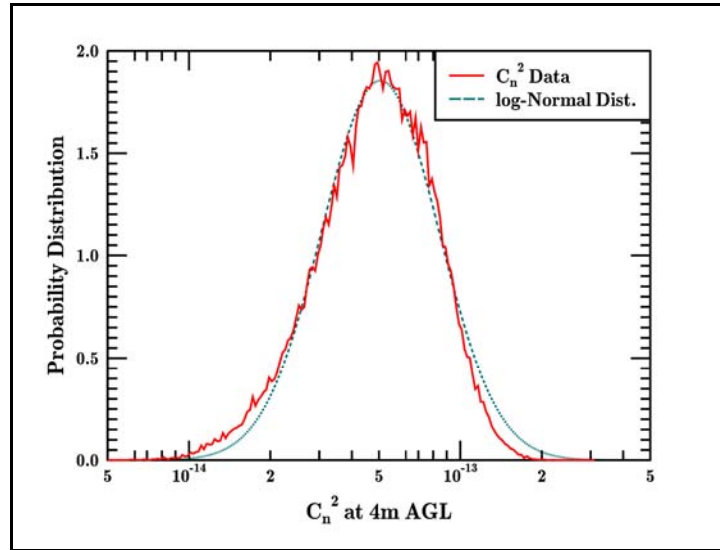

Figure 2. Comparison between measured C_n^2 data and modeled log-normal distribution of C_n^2 data.

In addition to the data, a log-normal distribution curve is plotted for comparison to the data. Analysis of the measured data indicated a log-10-mean value of -13.3186 ($C_n^2 = 4.8 \times 10^{-14}$), and a log-standard deviation of 0.215. However, as seen from the comparison between the plotted data and the theoretical log-normal curve, there is a slight skewness in the measured distribution. A better fit to the peak region of the data (as plotted) is obtained using an adjusted log-mean C_n^2 value of -13.295 ($C_n^2 = 5.1 \times 10^{-14}$).

The true C_n^2 distribution may or may not be log-normal. Further measurements are needed to establish whether observed skewness is characteristic of ensemble distribution deviations or simply anecdotal. Theoretically, there is some foundation for considering this assumption to be the correct one: The refractive index spectrum clearly exhibits power law dependence in its inertial subrange. Many of the factors controlling the strength of turbulence appear to be multiplicative in nature (additive in log space). Factors include wind driven mixing of air masses, solar radiation modulated by cloud cover, and surface reflectivity. Hence, C_n^2 variations could well represent a summation of log variable terms. Further, as discussed by Tatarskii (1961), the Rytov method is based on a log-amplitude analysis in evaluating propagation effects. Combining a series of along-path and environmental multiplicative effects and invoking the central limit theorem produces a Gaussian distribution in log space, to first order.

From a practical viewpoint, log coordinates are commonly used in plotting C_n^2. Considering vertical variations this is most reasonable because C_n^2 is proportional to pressure squared. Since pressure is approximately a logarithmic function of height, C_n^2 will also logarithmically decrease with height. C_n^2 is also a positive definite quantity. Plotting it in log space thus ensures that this condition is never violated. Lastly, C_n^2 measured near the surface often ranges over orders of magnitude over a diurnal cycle. Again, its natural environment is as a log variable. We will thus continue to employ a log-normal assumption until and unless it is shown to be untenable. Naturally, we will plot C_n^2 in terms of its log-mean. We express this using the expectation operator: $K = \left\langle \log_{10}(C_n^2) \right\rangle$. The angle brackets represent an ensemble average. By this we mean the average of all realizations of C_n^2 for a particular atmospheric condition.

The use of a log-normal distribution permits writing analytic forms for moments of the distribution, and the conversion of those forms to the scalar space used for performing the path integrations of equations 1–4. The log-normal distribution function for C_n^2 and a log variable x is written as,

$$p(x) = \frac{1}{\sqrt{2\pi}\,\sigma} \exp\left[-\frac{(x-\alpha)^2}{2\sigma^2} \right]. \tag{7}$$

Here, natural-log-based x has log-mean α and log-standard deviation σ. This density function is given as it appears in log space. To express the mean of this distribution in the linear space, define variable $y = \exp(x)$. The mean of y is found by integrating over the distribution and weighting this integral by y:

9

$$\langle y \rangle = \int_{-\infty}^{+\infty} \frac{e^x}{\sqrt{2\pi}\,\sigma} \exp\left[-\frac{(x-\alpha)^2}{2\sigma^2} \right] dx = \exp\left[\alpha + \frac{\sigma^2}{2} \right]. \tag{8}$$

Here, we note that $\langle y \rangle$ depends on both α and σ. This occurs because positive and negative fluctuations about the mean in log space do not have offsetting effects in linear space. Instead, asymmetries result, reflected by the offset term $\exp\left[+\sigma^2/2 \right]$.

Normally, C_n^2 is not given in terms of a natural-log variable. To transform to a base-10 logarithmic system we introduce the variable $w = 10^{x'} = \exp[x'\ln(10)] = \exp(\beta\, x')$; with $\beta = \ln(10) \approx 2.302585$. Variable x' can be related to the natural-log exponent x through: $x' = x/\beta$. With this substitution, the two systems can be compared by studying the probability that random variable X is between $x - dx/2$ and $x + dx/2$. The two probabilities should be equal in both systems, whereby,

$$p(x)\,dx = \exp\left[-\frac{(x-\alpha)^2}{2\sigma^2} \right]\frac{dx}{\sqrt{2\pi}\,\sigma} = \exp\left[-\frac{(x/\beta - \alpha/\beta)^2}{2\sigma^2/\beta^2} \right]\frac{dx/\beta}{\sqrt{2\pi}\sigma/\beta}$$
$$= \exp\left[-\frac{(x'-\alpha')^2}{2\sigma'^2} \right]\frac{dx'}{\sqrt{2\pi}\sigma'} = p(x')\,dx'. \tag{9}$$

The form of the probability density function is thus invariant under the transformation $x \to x'$.

Nevertheless, the expression for mean w becomes,

$$\langle w \rangle = \int_{-\infty}^{+\infty} w(x')\,p(x')\,dx' = \exp\left[\alpha + \frac{\sigma^2}{2} \right] = \exp\left[\beta\alpha' + \frac{\beta^2\,\sigma'^2}{2} \right] = 10^{[\alpha'+\beta\sigma'^2/2]}. \tag{10}$$

Here, $\langle w \rangle$ is the mean value in scalar space, while α' and σ' are statistics in log-base-10 representations, such as were evaluated based on the data shown in figure 2.

Let us now consider our application cases. In the first case we consider an LOS nearly horizontal to the ground. Given this LOS, and observer and target heights, we may evaluate a log-mean C_n^2. We then make a random draw on a zero mean Gaussian distribution, scale this result by the log-standard deviation of the fluctuations, add the log-mean C_n^2, and raise the result to a power of 10. Alternatively, rather than exponentiating (a relatively expensive calculation), we may simply do a table lookup given the log-value of the Monte Carlo generated C_n^2. From figure 2 we have a sample value of β (more will be discussed regarding this value). We then need values of mean C_n^2 along the path. This is the subject of much of the remainder of this report.

In the second case, we consider downward looking paths involving observing UAV platforms. In this case we assume that we are looking through enough statistically independent regions of

turbulence that the fluctuations will average out to ignorable fluctuations in the overall statistics. Thus, all that is needed is the average C_n^2 along the path, which necessarily requires inclusion of the factor $\exp\left[\sigma^2 / 2\right]$ in calculating the final mean value. From data plotted in Beland (1993), we find that each of these statistically independent regions is approximately a layer 200–300 m thick. A UAV flying at 2 km (6000 ft) AGL would be viewing the surface through 6–10 of these independent regions and thus would experience far less variations than ground-to-ground viewers.

To see this reduction in fluctuations explicitly, consider a downward view geometry in which the LOS passes through N statistically independent sections of the atmosphere. We can then evaluate the average C_n^2 over the path in a manner similar to the means of averaging the variable w above. The net standard deviation (σ_w) of w is found through direct evaluation using the rules for translating the log-normal statistics to the scalar realm:

$$\sigma_w^2 = \left\langle w^2 \right\rangle - \left\langle w \right\rangle^2 = \exp(2\alpha + 2\sigma^2) - \exp(\alpha + \sigma^2 / 2)\exp(\alpha + \sigma^2 / 2)$$

$$= \exp(2\alpha + \sigma^2)\left[\exp(\sigma^2) - 1\right] = \left\langle w \right\rangle^2 \left[\exp(\sigma^2) - 1\right]. \quad (11.A)$$

Taking the root,

$$\sigma_w = \left\langle w \right\rangle \sqrt{\exp(\sigma^2) - 1} \approx \left\langle w \right\rangle \sigma = \beta\,\sigma'\left\langle w \right\rangle, \quad (11.B)$$

assuming small σ, such that $\beta\,\sigma' << 1$.

As an example of the accuracy of this approximation we consider the value $\sigma' = 0.215$ found from the data plotted in figure 1. We then have $\sigma = 0.495$ and $\sigma_w = 0.527\left\langle w \right\rangle$. In this case the approximate method is 6% in disparity from the exact formula. However, 6% is not particularly significant since the error in estimating mean C_n^2 (as observed in typical thermosonde data) is usually around 0.1 in log-10-space terms, or about a 26% linear space variation.

Using this approach we can translate from the log space representation to the linear space and apply the central limit theorem in handling the fluctuations over a path segment composed of N independent sample regions. From the central limit theorem we take the original independent sample standard deviation (σ_w) and create a net effective standard deviation over the entire segment, $\sigma_w' = \sigma_w / \sqrt{N}$. Here, we express N as the number of independent height increments, ($N \approx \Delta H / 300\,\text{m}$) based on the height difference between the observer and observed objects, ΔH, and 300 m is a height increment over which C_n^2 obeys roughly uniform statistics of log-mean and log-variance, the aforementioned vertical correlation distance of "a few hundred meters."

We can use these statistics to either generate a single random variable representing the effective C_n^2 over a single altitude interval or adopt a mean C_n^2 value over an altitude range as long as the

11

number of independent intervals N is assumed large enough to sufficiently suppress the variance of $C_n{}^2$ over the interval. As an example, it will be shown that the mean $C_n{}^2$ over the interval 10–15 km AGL is roughly constant. Over this interval up to 16 independent segments with roughly constant $C_n{}^2$ are present. The $\sigma_w{}'$ for a path that spanning this region would thus be reduced roughly by a factor of 4 relative to a very short path within this region. The reduction is due to path averaging and is primarily for vertically oriented paths. For a log space standard deviation of roughly 1/2 a decade, we thus expect $\sigma_w{}' \approx 0.27$; that is, an average $C_n{}^2$ around 10^{-17} with a $\pm 27\%$ variation. We consider this value of $C_n{}^2$ to be relatively low compared to typical near-earth propagation paths. It may thus be feasible to handle the upper atmosphere using only mean values, reserving more explicit handling of path variability to LOSs close to the ground where fluctuation effects may have significant impacts. This is particularly important because ground-to-ground LOSs will be relatively short and thus will not experience $C_n{}^2$ variations much less than those observed in figure 2.

Also in figure 2, we note that the LOS was 950 m, at a 4 m height above surface over nearly flat terrain. For such a path we may evaluate the outer scale length of turbulence representing the longest correlations in the turbulent field. Analysis indicates this length is at most 100–200 m. Hence this 950 m path represents several coherence length intervals already. We thus may infer that for longer LOSs we can use the 950 m length result as a standard, and we can generate an $N = N_h$ tailored for a nearly horizontal propagation path scenario of

$$N_h \approx INT\left\lfloor \sqrt{1 + (L/950)^2} \right\rfloor . \tag{12}$$

This equation provides reasonable asymptotic behaviors that result in $N_h \to 1$, as $L \to 0$, and $N_h \to L/950$, as $L \gg 950$, as required.

To conclude this section, if we know what the log space $C_n{}^2$ distribution function looks like (in particular, if we know its log space standard deviation), then we can correct its mean value prediction in linear space by offsetting it by the factor $\exp(\sigma^2/2)$. Information available from vertical profile measurements of $C_n{}^2$ taken in New Mexico (such as data presented in Beland's, 1993, figures 2.14 and 2.15) indicates variability of $C_n{}^2$ by factors of around 2 to 3 throughout its entire range. Further evidence from Kunkel et al. (1981) indicates the main increases in variability occur near the boundary layer inversion. This likely occurs at night as well, and may indeed explain why modeling the nocturnal inversion in the boundary layer has produced so many uncertainties in the past.

4. The Surface Layer

Now that we have discussed the general nature of the C_n^2 probability density function, as well as general vertical model features, we are prepared to discuss the various segments of the atmosphere and model each segment. To do so, we need to understand the dominant physical processes in each altitude region. Typically, meteorologists begin by describing the largest scale effects and progress toward the smallest energy and size scales. However, for turbulence, surface based small scale effects are critical. We therefore begin our discussion at the ground and progress upward through the boundary layer and into the upper troposphere. This approach reflects the daytime behavior of vertical C_n^2 structure in that the surface value of C_n^2 actually drives the turbulence profile throughout the surface layer and into the boundary layer. On the other hand, behaviors in the upper troposphere are relatively insensitive to surface values, but still need to be coupled into the lower tropospheric model of C_n^2.

Ultimately, we need to consider two different coupling models between the boundary layer and the upper troposphere. Currently, we only know the form of this coupling for the daytime case, which is the focus of this first report. However, in the surface layer, that portion of atmosphere from the ground up to approximately 100 m, we can describe two different vertical profile models: a stable (nighttime) model and an unstable (daytime) case. The terms stable and unstable relate to the effects of buoyancy. During the day, displaced parcels of air tend to accelerate vertically away from their altitude of origin (they are unstable). At night, the ground is colder than the air above, due to surface radiative cooling, and parcels displaced vertically tend to oscillate about their height of origin. They exhibit stable vertical motion. However, from a modeling viewpoint, almost exactly the opposite is true. Due to the instability of air masses during the daytime, the boundary layer atmosphere becomes well mixed, and can therefore be much more easily characterized. Conversely, at night, due to the stability, different levels of the atmosphere become decoupled and small localized sources of energy perturbations (wave action, radiative emission, terrain discontinuities, etc.) become significant as the motions appear to fall into dynamically chaotic patterns. Hence, we currently will focus on only the daytime model once outside the surface layer.

We therefore begin characterizing the atmosphere starting at the bottom and progressing upward through the boundary layer to the upper troposphere. Previously, we found that Wyngaard's daytime free-convection $z^{-4/3}$ model matched the H-V model at 133 m. Below this altitude the H-V model shows only moderate increases of C_n^2 as one approaches the surface while the free-convection model shows C_n^2 increasing significantly toward the ground. This is our region of key interest since it is where most land combat occurs. We will apply similarity theory (Haugen, 1973) to describe the variation of C_n^2 with height in this region. Wyngaard (1973) provides us with the height dependence

$$C_n^2 \propto z^{-2/3} \left[1 - 7 \frac{z}{L_{Ob}} \right]^{-2/3}, \tag{13}$$

within this region during the unstable (daytime) conditions (where $L_{Ob} < 0$), and

$$C_n^2 \propto z^{-2/3} \left[1 + 2.4 \left(\frac{z}{L_{Ob}} \right)^{+2/3} \right], \tag{14}$$

under stable (night) conditions ($L_{Ob} > 0$).

During the day C_n^2 assumes a $z^{-4/3}$ height dependence for distances significantly above the surface. At night, C_n^2 takes on a vertical structure of $z^{-2/3}$ at $z = 0$, but rapidly decays to an approximately z-independent structure for large z. Under neutral density conditions $L_{Ob} \to \pm\infty$, resulting in $z^{-2/3}$ height dependence. However, the main problem in the surface layer is not in determining the height dependence, which is given, but rather in determining L_{Ob}, which is stability related. This parameter is usually derived based on other measured meteorological measurements. We must therefore consider its evaluation in detail in the next section.

4.1 Similarity Theory

Similarity theory assumes wind and temperature profiles near the surface are *similar* under comparable stability conditions. It is also assumed that certain stability-dependent derived quantities (scaling potential temperature θ_*, friction velocity u_*, and Monin-Obukhov length L_{Ob}) parameterize the vertical structures of temperature and wind speed in the surface layer. These parameters are related to the vertical fluxes of sensible heat and momentum, both of which are considered to flow vertically at constant rates through the surface layer.

Of these key parameter, the Monin-Obukhov length (or simply the Obukhov length) is fundamental in producing a dimensionless vertical parameter $\zeta = z / L_{Ob}$. To evaluate the Obukhov length, we begin with its canonical expression (e.g., Paulson, 1970):

$$L_{Ob} = \frac{u_*^2 \, \theta}{k^2 \, g \, \theta_*}, \tag{15}$$

where k is the dimensionless von Karman's constant (a dimensionless coefficient having the value of approximately 0.4 over typical terrain). The coefficient g is the acceleration due to gravity [9.8~m/s^2], and θ is the potential temperature [K] at reference height z_r. For heights close to the surface $\theta \approx T$.

Friction velocity u_* is defined as

$$u_* = \frac{k\,u}{\ln(z_r / z_0) - \psi_1} \, , \qquad (16)$$

where u is the wind speed [m/s] at height z_r, z_0 is the surface roughness height (the projected height at the wind profile indicates the speed should equal zero inside the roughness canopy. Usually z_0 is given as a function of the height of the *dominant* vegetative elements (Hansen, 1980). Lastly, ψ_1 is the stability-dependent diabatic influence function of velocity. It measures the deviation of the profile from log linear relationship.

In a *similar* form, the scaling potential temperature is given by,

$$\theta_* = \frac{\theta - \theta_0}{\ln(z_r / z_0) - \psi_2} \, , \qquad (17)$$

where θ_0 is the air temperature at the roughness height, and ψ_2 is the diabatic influence function of temperature. Usually θ_0 is difficult to predict because it does not occur at a specific surface. Rather, it is representative of the equivalent effects of the surface temperatures of the bare ground and foliage (leaf, stem, and twig) surfaces.

The thickness of the surface atmospheric layer is approximately twice the Obukhov length. However, we expect that the surface layer will be considerably less than the overall depth of the boundary layer, z_i [m], technically the base height of the elevated inversion layer during the day, or the thickness of the surface-based inversion at night. We use the symbology Z_i to denote the same quantity measured in km.

To determine the typical range of values for the surface layer thickness, we estimate the Obukhov length under various atmospheric conditions. Our estimation technique computes equations 15–17 while (for the moment) setting functions ψ_1 and ψ_2 to zero (their neutral condition limits). We use reference height $z_r = 2\,\mathrm{m}$ AGL and a roughness height of $z_0 = 5\,\mathrm{cm}$. The latter value for profile data collected in approximately 1-m tall desert scrub taken in the same area associated with the turbulence data taken in figure 2. Therefore, we find $\ln(z_r / z_0) \approx 3.7$, which is relatively large compared to either of the ψ correction terms. Let us next consider typical wind speeds to range from 1 to 5 m/s. We limit this range because larger wind speeds would suppress the temperature differential at the surface, while smaller wind speeds cause the results to diverge. For this range of the parameters, we find u_* values between 0.1–0.5 m/s.

For the range of θ_* we must consider what would be typical temperature differences during the day and night. During the day, a temperature drop of 1–15 K (weak to strong) between the surface and 2 m is not unusual. On the other hand, at night the temperature increase between the

surface and an observation height is not as strong because the energy exchange mechanisms at the surface are not as significant. Consider, then, temperature increases between +1 K and +5 K (positive because the surface is colder than the air at 2 m). For the sake of comparison we will also replace θ_* by $T_* = k\theta_*$, an alternative form of the scaling temperature sometimes found in the literature (e.g., Hoffert and Storch, 1979). From equation 17, we find T_* varies from -1.5 K to +0.5 K.

Assuming $\theta \approx T \approx 300\,\mathrm{K}$, we construct table 1 to illustrate the range and variability of L_{Ob}.

Table 1. Range of Monin-Obukhov Variability with Surface State.

u_*	$T_* = k\ \theta_*$										
	+0.5	+0.3	+0.1	-0.1	-0.3	-0.5	-0.7	-0.9	-1.1	-1.3	-1.5
0.1	+1.53	+2.55	+7.65	-7.65	-2.55	-1.53	-1.09	-0.85	-0.70	-0.59	-0.51
0.2	+6.12	+10.2	+30.6	-30.6	-10.2	-6.12	-4.37	-3.40	-2.78	-2.35	-2.04
0.3	+13.8	+23.0	+68.9	-68.9	-23.0	-13.8	-9.84	-7.65	-6.26	-5.30	-4.59
0.4	+24.5	+40.8	+122	-122	-40.8	-24.5	-17.5	-13.6	-11.1	-9.42	-8.16
0.5	+38.3	+63.8	+191	-191	-63.8	-38.3	-27.3	-21.3	-17.4	-14.7	-12.8

From table 1 we see that in almost all cases $|L_{Ob}| << 100$ m. This implies that for the daytime case, the asymptotic $z^{-4/3}$ behavior given in equation 13 will be the norm for several hundreds of meters above the surface in the daytime mixed layer (this region is also referred to as the free-convection layer) prior to experiencing the influence of the top of the boundary layer. On the other hand, when $|L_{Ob}|$ is of the order of z_i, C_n^2 itself will have a relatively low value. That is, low C_n^2 levels are synonymous with near-neutral conditions. In these cases, the influence of turbulence will be low already, and hence our interest in its impact on sensor systems will be limited. That is, the systems will likely be range limited by some effect other than the turbulence.

At the opposite extreme, $|L_{Ob}| < 2$ m can only occur under very stable or unstable conditions. In these cases caution is advised, as some model premises may have been violated. In general, we also do not want $|L_{Ob}| < z_r$, since the surface layer is only valid below ~2$|L_{Ob}|$. The majority of these cases occur for low wind speeds. The daytime mixed layer generally prevents such conditions from arising because as the boundary layer becomes unstable, convective circulations develop which tend to create their own winds regardless of the overall synoptic weather state.

4.2 Minimum Parameter Calculations

It seems from the discussion above that $|L_{Ob}|$ never becomes really large. In general its magnitude does not exceed 100 m. Yet the problem of observationally evaluating L_{Ob} remains. Normally, one does not take measurements at more than one atmospheric level. Hence, methods to evaluate L_{Ob} based on temperature and wind measurements are generally difficult to perform practically in the field. We may relax these measurement requirements, however, by simplifying and constraining the conditions under which these calculations are made.

The goal of this paper is to provide a rapidly-executing turbulence profile model that operates from a limited set of input data. We wish to use the Obukhov length to predict the vertical profile of C_n^2 in a wargaming environment, using a user-input value of C_n^2 at some convenient reference level z_r. Therefore, we will now show that all that is needed to evaluate the vertical structure within the surface layer is 3 parameters: wind speed, u [m/s], a temperature, T [K], and a C_n^2 value [m$^{-2/3}$], all at the same reference height z_r. We also must know whether we are considering a daytime (lapse, unstable, $L_{Ob}<0$) condition or a nighttime (stable, $L_{Ob}>0$) condition, and the roughness length z_0.

We use the height of the dominant vegetation to estimate the roughness length parameter input, z_0. For example, at WSMR there may be several plant types occurring in a single area, and each has a separate average height, but there will be one that presents the most leaf surface area and consequently dominates the drag effects on the wind. To evaluate z_0, Hansen (1980) recommended the Kung (1961 and 1963) equation,

$$\ln(z_0) = -2.85 + 1.19 \ln(z_e) \quad \rightarrow \quad z_0 = z_e^{1.19} / 17.29 , \qquad (18)$$

where z_e is the average roughness element height [m]. Many authors also provide tables of roughness lengths (e.g., MacArthur and Haines, 1982).

The "neutral event" crossover times defined as times at which the upwelling and downwelling surface heat fluxes are equal, are convenient temporal dividing lines between the daytime and nocturnal domains in the behavior of boundary layer turbulence. Typically, clear sky neutral event conditions occur approximately 60 minutes after sunrise and 40 minutes prior to sunset.

With all our required input parameters defined, we now relate L_{Ob} to C_n^2, u, and T. To derive this relation, we begin by considering Wyngaard's (1973) full equations for C_T^2:

$$C_T^2 = T_*^2 \, z^{-2/3} \, 4.9 \times \begin{cases} \left[1 - 7.0 \left(\dfrac{z}{L_{Ob}} \right) \right]^{-2/3} , & L_{Ob} < 0 ; \\[2ex] 1 + 2.4 \left(\dfrac{z}{L_{Ob}} \right)^{+2/3} , & L_{Ob} > 0 . \end{cases} \qquad (19)$$

Kunkel and Walters (1983) provided a means of converting C_T^2 to C_n^2:

$$C_n^2 = C_T^2 \, \frac{A^2 \, P^2}{T^4} \left(1 + \frac{0.03}{B} \right)^2 , \qquad (20)$$

where $A = 79 \times 10^{-6}$ K/mb, and $B = H_s / H_\ell$ is the Bowen ratio of sensible heat flux, H_s, to latent heat of vaporization, H_ℓ, in the surface layer. For the cases of interest here, the Bowen

ratio term may be ignored, because we assume $B > 1$. Pressure (P [mb]) changes with elevation above sea level and weather conditions. T [K] changes as a function of height above the surface due to heating/cooling. It is important to retain these terms in any equation of C_n^2. Also, it is important to remember that this relation for C_n^2 is limited to the visible and infrared (IR) bands. We have ignored the effects of wavelength dependence in C_n^2 as these are relatively small and within the margin of error in C_n^2 itself.

Although we retain the pressure dependence in the equation, we do not expect at any particular measurement site that P will vary significantly under fair weather conditions. That is, we expect P variations of only a few millibars. As such, we do not expect pressure to significantly alter the calculation of C_n^2. Instead, daily order of magnitude C_n^2 variations due to variations in heating conditions are viewed as the chief source of variation. Thus, one can specify temperature, T, and site height above sea level (ASL) to estimate P. From these, and local time of day, one can estimate C_n^2. C_T^2 is then evaluated from equation 20. We then use equation 19 to predict T_*, and, in combination with equations 16 and 15, predict L_{Ob} based on T, u, and C_n^2. Eliminating C_T^2 from equation 20 we obtain,

$$C_n^2(z_r) \approx \frac{T_*^2}{T^2} \frac{A^2 \, P^2}{T^2} z_r^{-2/3} \, 4.9 \, F(z_r / L_{Ob}) \approx \frac{u_*^4}{k^2 \, g^2 \, L_{Ob}^2} \frac{A^2 \, P^2}{T^2} z_r^{-2/3} \, 4.9 \, F(\zeta_r), \quad (21)$$

where we have invoked $\zeta = z / L_{Ob}$, and,

$$F(\zeta) = \begin{cases} [1 - 7.0 \, \zeta]^{-2/3}, & L_{Ob} < 0 \,; \\ 1 + 2.4 \, \zeta^{+2/3}, & L_{Ob} > 0 \,. \end{cases} \quad (22)$$

Initially, we set $F(\zeta)$ to 1.0 (the neutral condition limit). We then solve equation 21 for L_{Ob} to obtain,

$$L_{Ob} \approx \pm \frac{k \, u^2}{g \, [\ln(z_r / z_0)]^2} \frac{A \, P}{T} \frac{1}{\sqrt{C_n^2 \, z_r^{1/3}}} \sqrt{4.9} \quad . \quad (23)$$

The sign ambiguity arises when we take the square root of equation 21. To eliminate this problem we introduce a unary stability condition operator, called $\pi_s = \pm 1$, -1 for daytime (unstable atmospheric conditions), +1 at night (stable atmospheric conditions). Predictions of π_s can be based on local times and dates using local sunrise/sunset times and offsets to estimate neutral event transitions. Adding this term to the right hand side (RHS) we obtain:

$$L_{Ob} \approx \pi_s \frac{k \, u^2}{g \, [\ln(z_r / z_0)]^2} \frac{A \, P}{T} \frac{1}{\sqrt{C_n^2 \, z_r^{1/3}}} \sqrt{4.9} \quad . \quad (24)$$

Following this initial estimate, L_{Ob} is refined through an iterative technique. In subsequent iterations, the previous L_{Ob} obtained is used to seed the $F(z_r / L_{Ob})$ and u_* equations. This technique was tested for a series of conditions. Problems primarily arose in conjunction with near neutral conditions. In these cases the number of iterations required to stabilize the results increased, but were still less than 100. In most cases eight digit accuracy could be achieved in as little as 3–6 iterations. For example, the unstable atmospheric case with $\pi_s = -1$, $u = 5.7$ m/s, T=294 K, and $C_n^2 = \times 10^{-13}\, m^{-2/3}$, stabilized within six iterations to an Obukhov length around $L_{Ob} \approx -41.6\, m$.

Once L_{Ob} is evaluated, we can immediately evaluate T_*,

$$T_* = \frac{u_*^2\, T}{k\, g\, L_{Ob}}, \tag{25}$$

and estimate the surface sensible heat flux,

$$H_s = -\rho\, c_p\, u_*\, T_* = -\rho\, c_p\, \frac{u_*^3\, T}{k\, g\, L_{Ob}},$$

where ρ is the air density and c_p is the specific heat of air at constant pressure. We include these last two relations for completeness because they suggest that the C_n^2 may be considered an essential measured quantity rather than merely an inferred parameter.

5. Convective Boundary Layer

The remainder of the boundary layer that lies above the surface layer is characterized by the diurnal variation of its stability. This layer has been called the "convective boundary layer" (CBL) under daytime conditions due to the dominance of convective action. However, it is often called the mixed layer because it features both upward and downward air motion associated with convective cell development. Within the layer a nearly constant potential temperature vertical profile prevails. The CBL's basic features are illustrated, for example, in figure 1.1 of Kaimal and Finnegan (1994).

Under nocturnal conditions, the daytime boundary layer subdivides into two segments–a surface based inversion termed the "stable boundary layer" (SBL), and a remnant of the daytime mixed layer representing the near adiabatic conditions termed the residual layer. The SBL is not as well characterized as the CBL due to the complexity of processes that establish its structure. We thus first discuss models and data relevant to analysis of the better understood CBL structure, and defer treatment of the SBL to a later section.

The vertical structure equations for the CBL are commonly expressed in two different forms (the Kaimal et al., 1976 and Kukharets and Tsvang, 1980 models), both mentioned by Beland (1993). The Kaimal et al. (1976) model (or KM model) first models the vertical structure of C_T^2, and then converts from C_T^2 to C_n^2 using equation 20 (which also implies knowledge of pressure and temperature profiles). The KM model is expressed as:

$$\frac{C_T^2(z)}{C_T^2(z_r)} = \begin{cases} [z/z_r]^{-4/3}, & 0.0 < z \leq 0.5\, z_i \\ [(z_i/2)/z_r]^{-4/3}, & 0.5\, z_i < z \leq 0.7 z_i \\ [(z_i/2)/z_r]^{-4/3}\, [z/(0.7\, z_i)]^3, & 0.7\, z_i < z \leq 1.0\, z_i \end{cases}, \qquad (26)$$

where z_r [m] again denotes a reference level, and z_i [m] is the height of the elevated inversion base. Typically the inversion occurs between 1–4 km AGL for New Mexico desert sites. Kaimal et al. (1976) compared this relation with data collected during the Kansas experiment (figure 7 of their paper), and the fit was very good.

Kunkel et al. (1981) also compared this model to measured data collected in southern New Mexico. Their results, illustrated in figure 3 below, generally verify the KM model. On the other hand, Burk (1981) and Moeng and Wyngaard (1984) compared the KM model against other data which tend to produce less reliable fits to this theoretical curve. Moeng and Wyngaard indicate that the basic KM relation is really only a particular case of a more general relationship between the rate of entrainment of air moving vertically within the CBL and available fluctuation energy (including effects due to sensible heat fluxes and surface drag forces). The Kunkel et al. (1981) data taken over southern New Mexico desert regions supports this observation by exhibiting greater log C_n^2 variance at and above the inversion base. Such increase likely arises due to overshoot of warm air masses penetrating through the inversion base height. The larger the buoyancy, driven by surface heating, the greater the momentum as the air reaches the inversion base. On the other hand, entrainment would tend to dilute these buoyancy effects. Also, due to momentum conservation, air must mix downward below z_i, increasing turbulence slightly below the inversion base as well. The KM model appears to do a good job of characterizing these desert effects for typical daytime desert atmospheric conditions.

However, the KM model does not provide information about the evolution of the daytime vertical structure starting from the morning inversion or its collapse prior to the evening neutral event. Additional information on these evolutionary stages is available in the High Energy Laser Handbook Empirical Model (HELHEM) (Kunkel et al., 1984).

HELHEM is a computer code written to implement vertical profiles or time series of C_n^2 as proposed in the High Energy Laser Propagation Handbook (Kunkel et al., 1984). The model developed in the Handbook consists of empirical critical parameter data collected at various sites on WSMR, NM, and the algorithm whereby these data are combined into a C_n^2 profile at a given time of day or a diurnal time series of C_n^2 at a given altitude. The algorithm calculates C_n^2 at a

20

reference level of 8 m AGL, using sinusoidal fits to climatological values for the daytime/nighttime maxima and neutral event minima.

HELHEM extends the vertical scaling schemes detailed in the Handbook so that vertical profiles near neutral event times are evaluated and stellar scintillometer profiles of C_n^2 at high altitudes are accommodated. C_n^2 values at atmospheric levels that lie between the diurnally varying boundary layer and the diurnally invariant (but seasonally changing) upper atmospheric levels are interpolated using criteria that depend upon time of day and the height of the inversion above the well-mixed layer. Because HELHEM is empirical, its domain of validity is limited to the clear days, moderate wind speeds and dry soil that are characteristic of the WSMR environment. The database and methodology upon which HELHEM is based date back to the mid-1970s through mid-1980s. The integration of this material into the current model will be the subject of a future effort. Substantial changes include the conversion of HELHEM from the original Pascal language encoding and ensuring consistency with more recent measurements and theory.

The KM model, a form of which exists in HELHEM, is a useful tool for describing the vertical structure of C_T^2 within the boundary layer. Unfortunately, the KM model and its supporting data in the Kaimal paper only consider altitudes up to the base of the elevated inversion layer. The Kunkel et al. (1983) paper includes data extending to $1.5\, z_i$. These data are useful in assessing an adaptation of the Kaimal model made by Kukharets and Tsvang (1980) (hereafter, KT) that uses a Gaussian function to model the increased C_T^2 at the inversion interface. A comparison between the KM and KT models is illuminating. In KM, a C_n^2 value is required at reference level z_r. In HELHEM this level is fixed at 8 m. The user is permitted to input the inversion layer base height (z_i), if known. This quantity can be directly interpreted from an analysis of rawinsonde temperature data. In lieu of this knowledge, we devote section 5.1 of this report to an analysis of archived WSMR z_i data sets. Similarly, Kunkel et al. (1983) provide a number of referenced methods for estimating z_i. HELHEM encodes average layer depths for the WSMR area. Both the KM and KT models require a knowledge of z_i, but KT originally required a specific reference level value of C_n^2 at height $z_x = 0.1\, z_i$. Murphy et al. (1985) subsequently adapted the basic KT model for use with an arbitrary reference level. The modified relation is then given by

$$\frac{C_T^2(z)}{C_T^2(z_r)} = \left(\frac{z_i}{10\, z_r}\right)^{-4/3}\left[\left(\frac{10\, z}{z_i}\right)^{-4/3} + 0.6\exp\left\{-12\left[\frac{z}{z_i} - 1.1\right]^2\right\}\right]. \quad (27)$$

In effect, the factor $\left(z_i / 10\, z_r\right)^{-4/3}$ renormalizes the input value of C_n^2 at z_r to the original KT model's $z_x = 0.1\, z_i$ level. We can express the KT Gaussian peak width in terms of a standard deviation, which we will call σ_{KT}. We can write the exponential as $\exp\left\{-\left[z - 1.1\, z_i\right]^2 / 2\, \sigma_{KT}^2\right\}$, such that $\sigma_{KT} = z_i / \sqrt{24} \approx z_i / 5$.

21

Comparison of the KM and KT profiles reveals that between $0.7\,z_i$ and z_i the KM profile increases by the factor 2.92, while between $0.5\,z_i$ and $0.7\,z_i$ the KM profile is constant. At $0.5\,z_i$ the KT profile is 0.125 of its value at $0.1\,z_i$, and by $0.7\,z_i$ this factor increases to 0.163. The value increases further, to 0.578 at z_i, a factor of 3.55 larger than its value at $0.7\,z_i$. The relative increase factors between $0.7\,z_i$ and z_i are thus similar for the two profiles, but the KT profile continues to increase with altitude above z_i to its peak at $1.1\,z_i$. This behavior does not fit well with data presented by Kunkel et al. (1981) (hereafter, simply Kunkel data) that clearly shows a peak around $0.95\,z_i$, followed quickly by a decreasing profile, essentially returning to the previous $0.5-0.7\,z_i$ minimum values by $1.3\,z_i$. Burk (1981) shows similar behaviors for several data sets collected over ocean areas.

As presented by Beland (1993), the KT model was written for $C_n{}^2$ rather than $C_T{}^2$. We will attempt to use the concept introduced by KT of a Gaussian peak, but not focus on the exact functional form they suggest. In particular, the width of the KT peak, as indicated above, is $\sigma_{KT} \approx z_i /5$. The Kunkel data suggest the Full-Width-Half-Max of the inversion peak in log space is approximately $0.3\,z_i$, or $\sigma_K \approx 0.1274\,z_i \approx z_i /8$. Data presented in Beland (1993) and Burk (1981) tend to corroborate this narrower peak. Therefore, both the position and width of the peak in the KT model appear at variance with the measured data, but it should be noted that variations do occur in the measured data. Nevertheless, we will use the Kunkel data as a guide along with adding a Gaussian peak in log space to characterize the impact of the increased turbulence at the elevated inversion height. These considerations lead to the expression,

$$X_K(z) = \log_{10}\left(C_T^2\right) = \log_{10}\left(C_{TS}^2\right) + 0.775 \exp\left[-\frac{(z-0.95\,z_i)^2}{2\,(z_i/7)^2}\right]$$

$$+ \left[\frac{1}{3} + \frac{4}{3}\log_{10}\left(\frac{z}{z_i}\right)\right]\sigma\left[\frac{z_i - z}{z_i/8}\right], \quad (28)$$

where $C_{TS}{}^2$ is the $C_T{}^2$ value produced by surface layer equation (19), and $\sigma(z)$ is akin to the sigmoidal functions used in neural networks, given by,

$$\sigma(z) = \frac{1}{1 + \exp(z)}. \quad (29)$$

It has the properties $\sigma(z) \to 0$ as $z \to +\infty$ and $\sigma(z) \to 1$ as $z \to -\infty$.

The net effect of these expressions is that the first term on the RHS of equation 29 generates the surface layer effect when near the ground. The second term is the Gaussian at the inversion level. The third term has the effect of neutralizing the general $z^{-4/3}$ height dependence above the inversion layer. Figure 3 compares this proposed vertical profile with the Kaimal equations, the KT expression, and data presented in Kunkel et al. (1981). In the figure $C_T{}^2$ is presented in

normalized form according to its value at z_i. This comparison highlights the transition from the C_T^2 constant zone between $0.5\,z_i$ and $0.7\,z_i$ according to the Kaimal theory and the increased value at the inversion base. Note in figure 3 that each curve's data are normalized to the C_T^2 values at the inversion base ($z = z_i$).
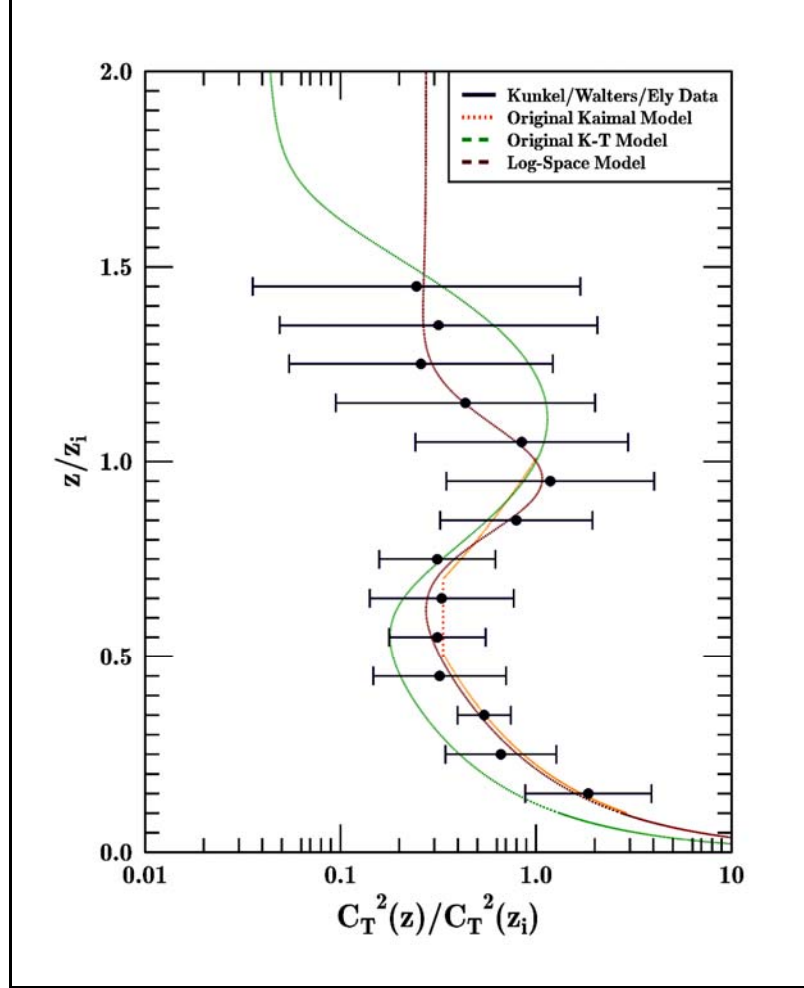

Figure 3. Kaimal family representations of C_T^2 compared to data presented in Kunkel et al., (1981) where data are normalized to a value of 1 at the inversion base ($z = z_i$).

Note that the Kunkel data represents an average formed from data taken during flights on eight different days spaced over a year's timeframe (1977–8), all collected at around 1200 local time. Uncertainty in the mean was estimated to be a factor of ~1.5 (0.18 in a log-10 representation) based on $\exp(\sigma/\sqrt{N})$. The standard deviations increase markedly (greater uncertainty) around the inversion base height and above. We may infer that this increase in variability is at least partially due to diurnal changes in entrainment to flux ratios as noted by Wyngaard and Moeng (1980). This same variability would not influence the lower boundary layer. As is evident from the data, at these lower altitudes the deviations are markedly reduced. If we then remove this

level of variation from the upper level standard deviations, we can estimate that perhaps half the variance (or more) is caused by uncertainties due to the entrainment.

Though the KT model does not appear to fit as well to the data as the proposed function of equation 29, it still remains marginally within the error bounds of the data. It has the same $z^{-4/3}$ behavior as the KM model up to $0.5\,z_i$. Its chief problem occurs following application of the normalization due to the positioning and magnitude of its peak. It is possible that the differences among the KT results, the KM model and the Kunkel data may relate directly to the environment in which the data were taken or the model developed.

The KM model was based on the 1968 Kansas experiment, a series of measurements conducted in essentially a grassland environment. The Kunkel data were taken over a desert basin. The Kukharets and Tsvang (1980) data were collected in the summers of 1976 and 1977 over the forested region surrounding Tomsk and the steppe region near Tsimlyansk. Different characteristic entrainment effects may have been operating for the KT measurements than for the Kansas experiment and Kunkel measurements. As for the KM model, it appears to fit the Kunkel data very well below z_i. Its match is, in fact, even better than as reported by Kunkel et al. (1981), since their normalization was to a C_T^2 value near the top of the surface layer. The normalization used in this report does lead to an improved fit. Since the profile proposed here extends beyond the inversion base height, however; it is believed to be more useful than the original KM model.

5.1 Daytime Boundary Layer Development

With the KM model we have the capability of modeling the structure of C_n^2 within the surface layer, mixed layer, and through $\sim 1.5\,z_i$. However, a key unknown as yet undiscussed is the height of the mixed layer itself. While the HELHEM model encodes mixed layer heights (as plotted in figure 4), these results reflect varying meteorological conditions and hence are not uniformly varying (which is illustrated in the subsequent analysis).
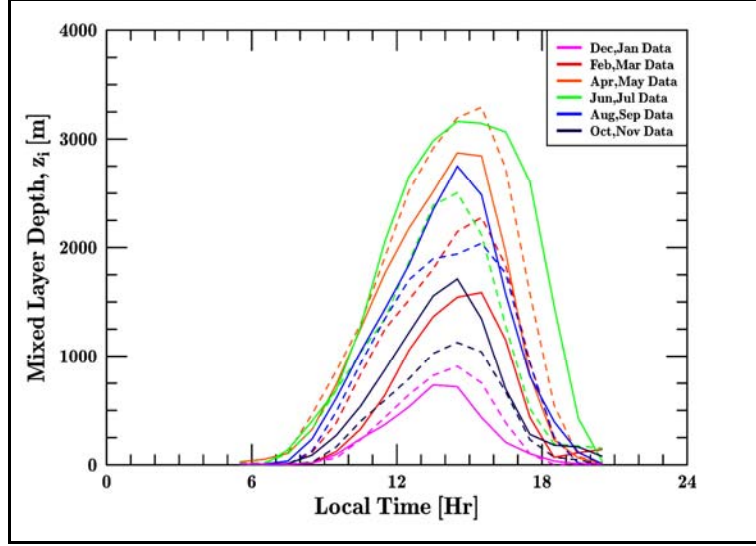
Figure 4. Norton and Hoidale (1975) data for second quartile (50% probability)
height of mixed layer, z_i [m].

Data for each line color group are organized as a solid line for the first listed month and a dashed line for the second listed month. A cursory study of the daily peak heights shows that December is the lowest curve. Curves for successive months show a steady increase in the maximum mixed layer depth through May/June. Peak heights then decrease approximately uniformly, except that the July and August data appear out of order because of summer monsoon effects which impact WSMR in July. These effects influence the positioning of the quartile data to higher average cloudcover conditions for July.

These data are based on the sets of aggregated z_i data generated for the WSMR region by Norton and Hoidale (1975). The statistics plotted are the second (2nd) quartile or 50% mark in the distribution of mixed layer heights. Thus 50% of the available data have mixed layer heights less than the indicated value and 50% have layer heights which are greater. In the Norton and Hoidale (1975) data 1st and 3rd quartile results were also illustrated. From these plots, the 1st quartile appear to have layer heights approximately 80% the height of the 2nd quartile while the 3rd quartile represent heights approximately 125% of the height of the 2nd quartile.

Based on these plots of z_i several features are apparent. First, the height of the mixed layer appears to rise following sunrise and fall prior to the evening neutral event. This behavior appears to contradict the behavior illustrated in figure 1 where the mixed layer abruptly develops into the residual layer around the time of the evening neutral event. Apparently the true behavior is that the residual layer develops gradually, starting at the entrainment zone and building gradually downward toward the surface. This is due to the surface heating gradually diminishing throughout the afternoon as the solar zenith angle increases. The solar input therefore can only support a diminished mixed layer thickness as the zenith angle increases. Second, we notice that the slope of the increase in the layer thickness is more gradual in the morning than the rate of

height collapse in the afternoon. A symmetric function of height with time thus does not seem appropriate.

The goal of this analysis is to provide a numerical model for the mixed layer depth, z_i, that smoothly varies from month to month, as well as according to the time of day. Since the daily time dependence follows an approximately bell-shaped (Gaussian) curve, we start with this model. We then note that the effect of the asymmetry is similar to a slightly cresting wave. To simulate this effect, we can shift the curve over slightly, as a linear function of height, to express the asymmetric effects. We simulate these two influences with the function

$$z_i = A\ y = A\ \exp\!\left(-\left|x - cy\right|^b\right),\tag{30}$$

where x is a normalized time of day which is zero sometime around the peak time of each curve. Normalized height y is used so that we can decouple the curve peak value (A) from the characteristic curve shape as a function of time of day. Peak height is then modeled as a function of the time of the year: $A = A(M)$, where we introduce M as a floating point month variable: $M = (J_d - 15)/365 \times 12$, generated using J_d, the current Julian date. We ensure that $(x - cy)$ is positive valued by imposing the absolute value symbol in order to ensure that the argument of the exponential is real valued. This is necessary because in general $b \neq 2$, as it would be if the diurnal curve exactly fit a Gaussian profile. If $b \equiv 2$ then $(x - cy)$ always squares to a positive number.

Because the curves are skewed, we need y (proportional to z_i) to produce a skewness tilt to the result. But this results in y appearing on both sides of the equation. The equation must therefore be solved iteratively. Yet we anticipate that the skewness (tilt) parameter c will be small. In this case, only a few iterations should be necessary for convergence.

Having posited a form for our solution, we now need to analyze the available data to evaluate parameters $A(M)$, $b(M)$, and $c(M)$. We begin with parameter $A(M)$. Figure 5 plots the maximum daily heights associated with the 2nd quartile daily mixed layer depth data for each month. We have developed three candidate fits to this data which are illustrated in figure 5. These curves are given by the equations,

$$A(M) = \begin{cases} 2100 + 1300\sin\!\left[2\pi\,(M - 3.0)/12\right] \\ 2080 + 1120\sin\!\left[2\pi\,(M - 2.9)/12\right] \\ 2080 + 1120\sin\!\left[2\pi\,(M - 2.9)/12\right] + 220\sin\!\left[2\pi\,(M - 2.3)/6\right] \end{cases}.\tag{31}$$

The red curve (1st equation above) exhibits a simplified fit. It ignores drops in layer heights in June and July which are likely related to monsoon activity. The red curve thus best represents dry soil conditions, and characterizes scattered cloud cover conditions as further described below. The blue curve (2nd of equation 32) is a two-term least squares fit to the actual data. The green curve (3rd of equation 32) is a three-term least squares fit. This latter fit better accounts for

26

average declines in mixed layer heights during monsoon periods, though, being an average, it does not reflect the actual condition on any particular day.
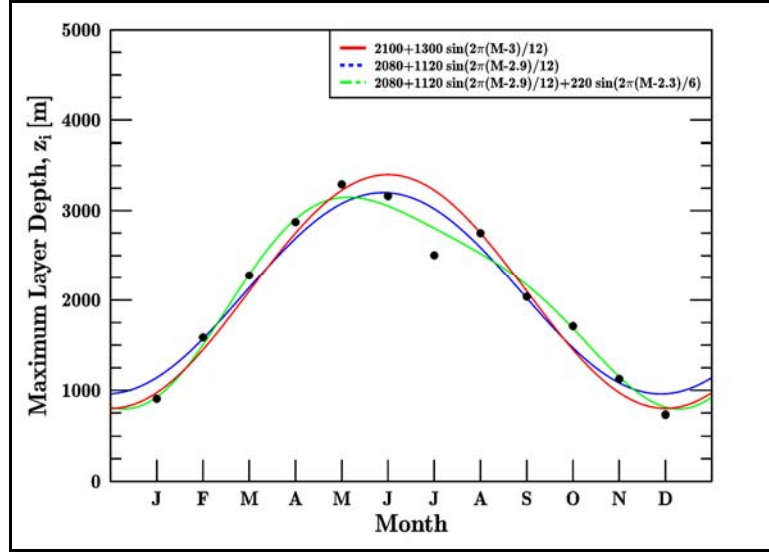

Figure 5. Three plotted fit models to the monthly 2nd quartile daytime maxima from Norton and Hoidale (1975) data of mixed layer height, z_i [m].

For our purposes we chose the red curve. A key reason for selecting this curve is related to the climatology of cloud cover for the site. From the climatological cloud cover data collated by Hoidale and Newman (1974) for the WSMR, NM, site, based on the 1951–1973 period clear or scattered (up to 50%) cloud cover conditions were present over 60% of the time. Hence, for most months the 2nd quartile daily maximum data would fall within the scattered cloud cover condition.

We also considered the interaction of climatological averages of cloud cover with the statistics plotted in the 2nd quartile statistics modeled. However, during the months July and August, the fractional cloud cover markedly increases, on average. Thus, clear sky conditions, which average around 37% of each month, drop to an average of 22% for July and August. When combined with the scattered percentages, the net cumulative probability of cloud cover less than 50% for July and August falls to less than 50% meaning the 2nd quartile data are associated with broken cloud cover conditions rather than scattered conditions. The red curve would then tend to better reflect the true height of the mixed layer for scattered cloud cover conditions throughout the year. Norton and Hoidale (1975) further report that 3rd quartile mixed layer heights are approximately 25% higher, while 1st quartile results are 20% lower. We can associate these differences in height with the effects of cloud cover conditions, permitting us to model both the height and effects of weather on the mixed layer height. Third quartile results (125% of equation 44) will thus be used for clear conditions (<10% cloud cover), while 1st quartile results (80% of equation 44) will be used for broken sky (60–90% cloud cover) conditions.

As the second phase in building the equation to predict the height of the mixed layer (equation 31), we need to know how to set up the x variable, which is a normalized time of day. The best means of accomplishing this task is to note that regardless of the value of the exponent b, whenever the argument $|x - cy| = 1$, we have a mixed layer height equal to $A e^{-1}$. Therefore, our next analysis will be to determine at what times of the day these e^{-1} of the 2nd quartile diurnal peaks occur. The data for these times, along with Fourier-fitted curves (using sinusoidal weighted fitting functions) of these data, are plotted in figure 6.
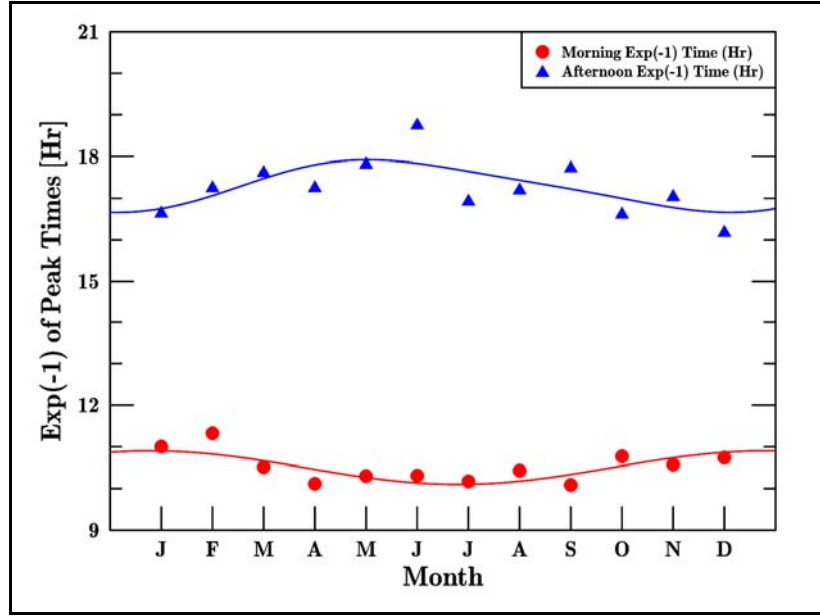

Figure 6. Interpolated times at which the Norton and Hoidale (1975) data for second quartile mixed layer heights equaled e^{-1} of the maximum monthly heights.

Morning curve is given by equation 33. Afternoon curve is given by equation 34.

As expected, in summer the e^{-1} points occur earlier in the day and later in the afternoon than during the winter based on the increased daylight time. Fourier analysis was again used to produce least squares fit equations: For the morning crossing times,

$$t_m = 10.5 + 0.4\sin[2\pi(M + 2.2)/12], \tag{33}$$

was found, where M is the same month variable described previously. For the afternoon crossing time the equation,

$$t_a = 17.3 + 0.6\sin[2\pi(M - 2.6)/12] + 0.1\sin[2\pi(M - 2.5)/6], \tag{34}$$

was obtained. For the afternoon event the second Fourier sine term is needed primarily to account for effects of July and August monsoon clouds. However, in this case, the means of removing the cloud cover effects are less obvious, and thus the equation containing the effects was retained.

We thus now have two parts of formula for predicting the mixed layer height, but we still need to know the degree of the skewness of the curves in order to decouple the cy term from the x term so we can know how to normalize the time. This step equates to evaluating the constant c.

To do this, we analyze the derivatives of equation 31 at the points $z_i = Ay = Ae^{-1}$. But before we can look at the derivatives, we need to consider another problem first: We have written equation 31 in terms of a normalized time, x. But, we do not yet know how to normalize x. To first perform this normalization, we consider the argument values of the exponential when the mixed layer equals Ae^{-1}: When this condition occurs, the argument value must equal $|x - cy| = 1$. But for this case, we know $y = e^{-1} = 1/e$. We thus have $|x - c/e| = 1$. Now, we expect that the normalized time x is centered around the noon timeframe. Thus at the morning e^{-1} time, $x < 0$, while in the afternoon, $x > 0$. We call the morning time x_m, so that $x_m < 0$, and the afternoon time x_a, so that $x_a > 0$. Hence, we can write, $x_m - cy = -1$ and $x_a - cy = +1$. The difference $x_a - x_m$ must then be 2. We can then produce a linear model for the normalized time so that $x_a - x_m = 2$. This model is given by, $x = (t - t_0)/[(t_a - t_m)/2]$, where t is the actual local time in hours past midnight, t_m is the morning e^{-1} crossover time, t_a is the afternoon e^{-1} crossover time, and t_0 is an offset time close to noon that is yet to be determined. Even though we do not know t_0, we can show directly that inserting times t_m and t_a into the above definition results in $x_a - x_m = 2$.

From our newly defined x variable in terms of time t in hours, we can compare the derivative of equation 31 with the time rate of increase in height of the mixed layer at time t_m and, likewise, the time rate of decrease in z_i at time t_a taken directly from the Norton and Hoidale data. From the equation we have

$$\frac{dz_i}{dt} = \frac{dz_i}{dx}\frac{dx}{dt} = \frac{dy}{dx}\frac{2A}{t_a - t_m}.$$

From the data sets we obtain sample results for each month for both the morning and afternoon crossover times. We call these samples d_m and d_a data, respectively, which compare directly to the dz_i/dt values. We then normalize these statistics by multiplying by the quantities $(t_a - t_m)/2A$. This produces results comparable with dy/dx. These normalized data are plotted in figure 7.
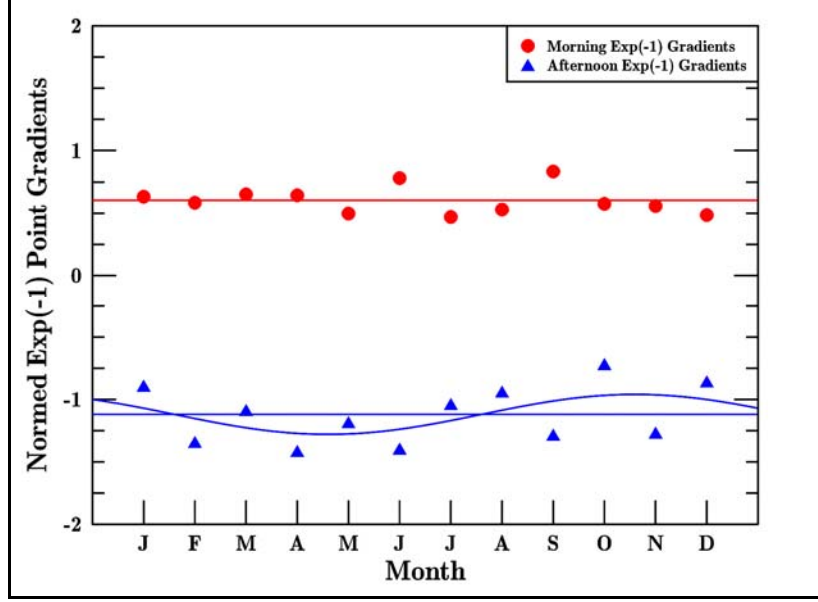
Figure 7. Normalized rates of rise (fall) in mixed layer height as a function of
month from Norton and Hoidale (1975) reported mixed layer 2nd
quartile depth data.

The curves plotted are given by equation 35. The curves used to model the crossover normalized gradients are,

$$g_m = 0.60; \qquad g_a = -1.12 + 0.16 \sin[2\pi (M + 4.4)/12], \quad (35)$$

for the morning and afternoon crossover point, respectively. Considering the amount of spread in the afternoon crossover data, it is perhaps better to use the constant 1.12, but there does appear to be a trend in the behavior at the crossover that is more than merely a constant effect. The consistency of the morning transition gradient appears indicative of the characteristic way surface heating *burns off* the morning inversion layer. By comparison, afternoon variability is likely due to the overall depth of the boundary layer, and the availability of late afternoon solar energy.

To use these results, we rewrite equation 31 as,

$$(-\ln y)^{1/b} = \pm(x - cy), \qquad (36)$$

where we use the positive branch when $x > cy$ and the negative branch when $x < cy$. Taking the derivative of both sides with respect to x we find,

$$-\frac{1}{b}(-\ln y)^{1/b-1} \frac{1}{y}\frac{dy}{dx} = \pm\left(1 - c\frac{dy}{dx}\right). \qquad (37)$$

30

Evaluating this result at $y = e^{-1}$ ($\ln y = -1$) we obtain,

$$-\frac{1}{b}e^1 \frac{dy}{dx} = \pm\left(1 - c\frac{dy}{dx}\right). \tag{38}$$

Now at the morning crossover we have $dy/dx = g_m$ and we use the negative branch. We thus have,

$$-\frac{e}{b}g_m = -1 + cg_m \quad \rightarrow \quad 1 = \left(c + \frac{e}{b}\right)g_m. \tag{39}$$

At the afternoon crossover we have,

$$-\frac{e}{b}g_a = -1 - cg_a \quad \rightarrow \quad 1 = \left(c - \frac{e}{b}\right)g_a. \tag{40}$$

We now have two equations in two unknowns. Solving, we find,

$$b = \frac{2e}{1/g_m - 1/g_a}; \quad c = \frac{1}{2}\left(\frac{1}{g_m} + \frac{1}{g_a}\right). \tag{41}$$

At t_m the argument to the exponential must equal -1. Similarly, at t_a the argument must equal +1. This leads to the transformation equation linking dimensionless time, x, to t.

$$x = 2\frac{(t - t_0)}{(t_a - t_m)} + \frac{c}{e}, \tag{42}$$

where $t_0 = (t_m + t_a)/2$. Altogether, then, we have equation 31 for the overall prediction equation for z_i. This equation uses equation 32 (first line) for A, equation 41 for parameters b and c, equation 35 for g_m and g_a, and equation 42 for x, based on t_0 from equation 41 and equations 33 and 34 for times t_m and t_a, respectively. These various relations are combined to illustrate the estimates of daytime variations of z_i as a function of month in figure 8.

We thus now have a viable model for daytime mixed layer depth, z_i, which provides the missing parameter needed for the boundary layer model given in equation 29. The next step is to link the equation 29 boundary layer model to an upper troposphere model based on the CLEAR I study. This step is performed in the next section.
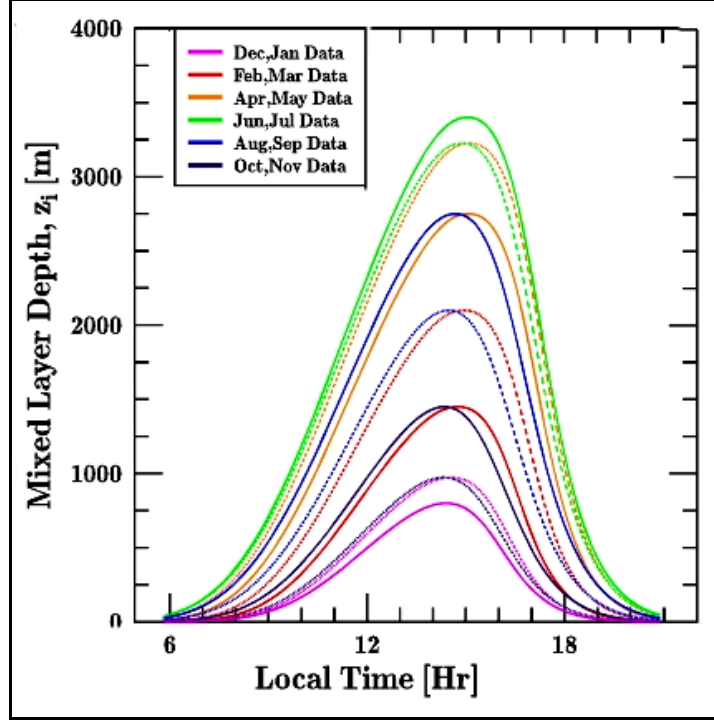
Figure 8. Combined predictions of mixed layer depth as a function of
month of the year based on Norton and Hoidale (1975) data.

6. The Upper Troposphere Profile

In section 1 we discussed the H-V model for vertical C_n^2 structure. Our chief interest was its
behavior in the boundary layer. However, while H-V may be the most widely cited model, other
profile models provide superior alternatives for modeling upper atmospheric C_n^2 structure. For
example, in the Submarine Laser Communication (SLC) studies model, Miller and Zieske (1979)
provide a complete piecewise continuous profile of C_n^2 starting from approximately 3 km ASL
up to 20 km ASL. SLC provides model profiles of C_n^2 for both day and night mean cases,
starting at 3 km ASL because the astronomical observatory for which the model was designed is
situated at the summit of a volcano 3 km ASL in Hawaii. This observatory is the Air Force's
Maui Optical Station (AMOS). Of critical interest, the SLC day and night models are identical,
starting at 1500 m AGL; that is, 4500 m ASL. This starting point is important because the
atmosphere 1500 m above a geographically isolated, 3 km-elevated island surface will be nearly
representative of an atmosphere 4500 m above the ocean. The fact that the SLC day and night
profiles are independent of time above a certain altitude provides justification for applying the
CLEAR I model results, obtained at night, to the daytime upper troposphere as well.

Beland (1993) discusses both the Air Force Geophysics Laboratory's (AFGL's) AMOS and the CLEAR I models. The AMOS model, taking its name from the observatory for which its profile was tailored, was an attempt to model characteristic C_n^2 vertical profiles for characterizing propagation effects for that particular site. The model results show similarities to the SLC model, but feature fewer gradient discontinuities in the vertical profile. Beland's (1993) discussion of these models is highly recommended reading, since it provides details of methods of data collection and limitations of the models. Subsequent to developing the AMOS profile, AFGL and the Army Atmospheric Sciences Laboratory studied vertical profiles of C_n^2 over the New Mexico desert for similar characterization purposes. The results of these studies were codified in the CLEAR I model. However, while both daytime and nighttime profiles were sought, the stellar scintillometers used to measure the profile shapes were inaccurate during daylight hours. Thus, only a CLEAR I night model was developed. This model is given by,

$$\log_{10} C_n^2(Z) = A + BZ + CZ^2, \quad 1.23 < Z \le 2.13, \quad (43.A)$$

where $A = -10.7025$, $B = -4.3507$, $C = +0.8141$;

$$\log_{10} C_n^2(Z) = A + BZ + CZ^2, \quad 2.13 < Z \le 10.34, \quad (43.B)$$

where $A = -16.2897$, $B = +0.0335$, $C = -0.0134$;

$$\log_{10} C_n^2(Z) = A + BZ + CZ^2 + D\exp\left\{-\frac{(Z-E)^2}{2F^2}\right\}, \quad 10.34 < Z \le 30, \quad (43.C)$$

where $A = -17.0577$, $B = -0.0449$, $C = -0.0005$, $D = -0.6181$, $E = 15.5617$, $F = 3.4666$. Z denotes height ASL in kilometers. The CLEAR I model starts at 1.23 km ASL because this is the surface elevation of the New Mexico desert basin.

The AMOS model was designed to treat a purely oceanic environment and the CLEAR I model was designed for largely continental conditions. Hawaii is in the tropics while New Mexico is a midlatitude continental location. Yet the two C_n^2 profiles for AMOS and CLEAR I are almost identical at altitudes above 10 km ASL (essentially the tropopause). The question therefore is whether we are comparing disparate conditions or whether the similarities in the two profiles at upper altitudes are characteristic of more underlying similarities in physics of the tropopause between the two sites.

Contrary to the similarities between these two profiles above 11 km ASL, major differences occur between the AMOS and CLEAR I profiles below 11 km. Briefly, these consist of steeply increasing turbulence in CLEAR I below 11 km as opposed to relatively constant turbulence in AMOS extending down to 5 km. Since we are interested primarily in desert/land scenarios we will henceforth focus on the CLEAR I model and linking this model into the boundary layer turbulence model of equation 29.

First, as discussed previously, CLEAR I is only available for nighttime conditions. Nevertheless, the SLC profiles show that the vertical C_n^2 behavior is insensitive to time of day at altitudes above 5 km ASL. Also, we have just indicated that the AMOS and CLEAR I profiles are virtually identical above 11 km ASL. These observations, combined with a personal communication with R. Beland indicate the following: Midlatitude C_n^2 profiles appear relatively time and location independent above 11 km ASL. Second, since diurnal forcing at the surface takes considerable time to transport vertically in the atmosphere, the CLEAR I night results should be applicable to daytime conditions above 5 km ASL as well. There may be seasonal variations in these statistics. Further research will be necessary to translate available data from additional sources into the context of the CLEAR I profile shape. The remaining step in this process is thus to connect our boundary layer profile model (equation 29) to the CLEAR I profile (primarily equation 43.C) starting at the top of the boundary layer (about 3 km AGL) and approximating the CLEAR I model starting in the mid troposphere (5 km ASL). We expect diurnal variations in C_n^2 will be largely confined to the boundary layer, since heating/cooling processes above the surface will not be strongly localized and hence sharp temperature/density gradients will not be driven by diurnal forcing effects.

The key feature of the CLEAR I night profile is its Gaussian peak placed at approximately 15 km (see equation 43.C). This peak marks the transition to the stratospheric inversion. To couple the boundary layer equation to the CLEAR I profile we choose to build a new profile equation which smoothly transitions to equation 43.C at high altitude. We then approximate equations 43.A and 43.B using our existing boundary layer equation plus new transition terms. However, we must first convert equation 43.C from its original form, where height appears in ASL form to an AGL form more suitable to wargaming applications. To do so, notice that to shift the height of the 15 km Gaussian peak all that is necessary is to adjust the constant E. The new value is set to $E = 14.3317$. Coefficients D and F need not be modified. The correction to E, a 1.23 km decrease, adjusts this height to reflect the surface height of southern New Mexico. Similarly, we correct coefficients A and B such that the intercept and slope of the C_n^2 profile evaluated using the old profile at a height of $Z = 1.23$ km generates the same results for the new profile when using $Z' = 0$ km. The modified values are $A = -17.1137$, and $B = -0.0461$. C does not need to be modified since the curvature of the profile is unmodified. The form of the new equation is identical to equation 43.C. The only differences are in the coefficients and the height parameter (renamed Z') which measures altitude above the surface. Henceforth we designate this modified version of equation 43.C) as the function $N_u(Z')$. We shall, however, simply write height as Z, dropping the primed convention, since the height will be assumed to be height AGL, not height ASL.

It also seems more realistic to seek a smooth function of altitude which approximates the CLEAR I profile but avoids the profile kink which occurred at 10.23 km ASL in the original model. We therefore propose the following equation to model the combined mid-level and upper-level CLEAR I function:

$$N_{mu}(Z) = N_m \, \sigma\left[\frac{Z - 7.8}{2.4}\right] + N_u(Z)\,\sigma\left[\frac{7.8 - Z}{2.4}\right] - 1.3\,\sigma\left[\frac{Z - 9.2}{1.6}\right]\sigma\left[\frac{9.2 - Z}{1.6}\right], \qquad (44)$$

where we introduce the fitting constant $N_m = -16.23$. This functional form replaces both equation 43.B and 43.C, and is based on height AGL. Figure 9 compares the new equivalent form of the CLEAR I model with results of the original CLEAR I profile's equations 43.B and 43.C offset in height by 1.23 km.
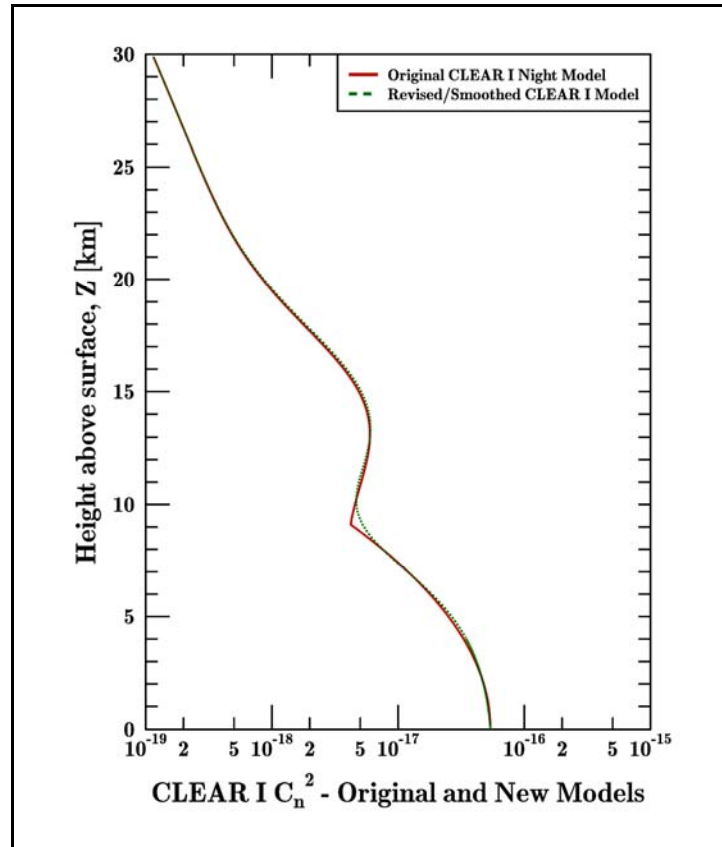
Figure 9. Plot of the upper two sections of the original CLEAR I profile
model and a revised/smoothed vertical profile approximation of
the same curve region.

We then simply need a set of profile equations that smoothly transition with the boundary layer. It is not necessary that we have a daytime upper troposphere model since, as previously shown, the nighttime model approximates the daytime case. However, we do need an appropriate transition model to connect the two model domains. We can perform this connection using a

pair of sigmoidal functions to splice the two together starting at approximately $2z_i$ and ending around 10 km ASL.

We therefore will use the function $N_{mu}(Z)$ (emulating the CLEAR I model's mid (m) and upper (u) portions) for heights above 10 km, and introduce the function

$$N_K(Z) = X_K(1000Z) + \log_{10}[A^2 P^2 / T^4], \qquad (45)$$

based on the Kaimal CBL model for heights below 3 km ASL. Here, N_K is a log-base-10 representation of C_n^2 generated based on equation 20. The C_T^2 input to equation 20 is provided by X_K from equation 29. Pressure and temperature inputs can be approximated by adiabatic atmospheric profiles where

$$T(Z) \approx T(0) - 6.455Z; \quad P(Z) \approx P(0)\exp(-Z/8).$$

Finally, the boundary layer and CLEAR I profiles terms can be combined using sigmoidal functions:

$$N(Z) = \sigma(Z - 7)N_{mu}(Z) + \sigma(7 - Z)N_K(Z), \qquad (46)$$

where $N(Z)$ now represents the log-base-10 mean C_n^2.

We compare the resulting vertical profiles created using this model for two examples. The reference level for both is $z_r = 2$ m AGL. The dashed (green) curve begins at a value of -12.2. The second solid (red) curve begins at a value of -12.7. The two curves are illustrated in figure 10. Due to the sigmoidal functions used, changes in the C_n^2 at low level only influence the boundary layer region.
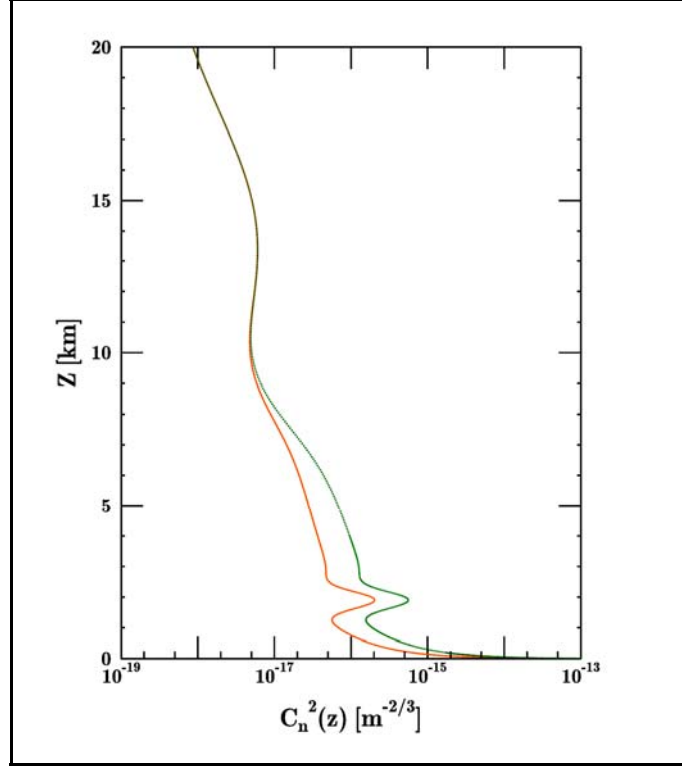
Figure 10. Comparison of daytime vertical profiles for cases with different reference level turbulence values, $\log_{10} [C_n^2] = -12.2$ (green dashed) and -12.7 (red solid).

Once the log-mean C_n^2 profile is known, we may evaluate the mean C_n^2 at any level via the formula (see equation 10),

$$C_n^2(z) = 10^{N(z)+\sigma^2(z)/2}. \tag{47}$$

Based on communications with R. Beland, the σ log-standard deviation appears to be a roughly constant factor of 2–3; that is, about 0.4 in its log representation, or an offset of $\sigma^2 / 2 \approx 0.1$. In other words, the variations do not appear, upon averaging, to be too significant.

7. The Stable Boundary Layer

We now briefly discuss modeling optical turbulence at night within and above the nocturnal boundary layer (NBL). The lowest portion of this layer is termed the SBL. This layer extends from the surface to the top of the surface based inversion, z_s. Above this layer, as illustrated in figure 1, are the residual layer and the capping inversion. Our goal is to link a model of the turbulence within the stable surface layer to a model of the overall boundary layer, and thereafter to the CLEAR I night model. Nominally, we already know the results for the surface and upper

troposphere regions at night. The only missing structure is the intermediate residual layer. This layer begins somewhere between 30 and 400 m AGL. This initial height depends on the thickness of the surface inversion which is an increasing function of height throughout the evening. The layer extends up to the capping inversion height that demarcates the top of the residual layer, 1–3 km above the surface.

Complicating this analysis are two issues. The first is a data gap. Since most applications looking to answer questions of layer structure have been associated with high energy laser (HEL) ground and airborne systems, the regions of the atmosphere studied, and the questions addressed, have been largely tailored to either very high altitude (30,000+ ft) long range horizontal propagation (airborne laser) or earth to space (free-electron or other ground based lasers). As such, the structure of the intermediate atmosphere has been handled mainly as a bulk quantity for only specific laser wavelengths. Second, for the information that does exist, only the integrated results were studied; that is, ground-based measurements of coherence diameter (r_0) and isoplanatic patch size (θ_0). From sporadic, largely anecdotal evidence (personal communication with R. Beland) we know the general standard deviation of the various layers outside the boundary layer are again log-normally distributed with standard deviation in the 2–3 range (log-based σ between 0.3 and 0.5). We also know that C_n^2 is a generally decreasing function of height, whose main driving dependence may be simply the overall rate of decline of pressure and temperature with altitude.

In section 5 we developed a C_T^2 model which coupled the predicted surface layer C_T^2 functionality to a known model of C_T^2 variation throughout the CBL, up to the base of the daytime entrainment zone. At night, the behavior of the vertical structure of C_T^2 is based more on smaller energy sources (wind driven mixing, gravity wave energy, etc.). These sources, while much less predictable, being also less energetic, may in some sense be viewed as perturbation mechanisms that exist at all times, but which only emerge as significant factors at night. While it is true that the variability of the C_n^2 increases at night, we postulate that a workable model for use in wargaming applications is possible.

Kaimal and Finnegan (1994) provided a survey of the NBL structure. According to their survey, the vertical structure of C_T^2 is described as "z-less" beginning at approximately $z = L_{Ob}$. This term "z-less" implies that the functionality does not depend on height z at all. According to Nieuwstadt (1984), z-less structure means C_T^2 depends on only local wind and temperature gradients at each level. These levels become decoupled from each other and from the ground due to the stable stratification in the ground-based inversion so that each level becomes independent of height z. On the one hand this makes a systematic model of the vertical dependence a problematic proposition. On the other hand, since the layers become decoupled, they are also cut off from sources of energy. We may thus look at the statistical distribution of energy in the different layers as a stochastic process. Equation 19 encodes this z-less relationship as best as possible using a z^0 limiting dependence for heights $z > L_{Ob}$, $L_{Ob} > 0$.

However, detailed studies of the stochastic nature of the intervening layers are largely lacking. Studies of these issues have devolved to studies of large eddy simulations (LES) of the boundary layer atmosphere. Due to the complexities of the LES modeling process much intense effort has been expended addressing these models in and of themselves and answering questions regarding the turbulence structure have been sidelined by other issues due to funding priorities, as must be expected. Yet the need remains for some proposed vertical profile model.

To provide such a model we begin with equation 19, which provides a vertical form for C_T^2 at night:

$$C_{TS}^2(z) = C_T^2(z_r) \frac{z^{-2/3}[1 - 7(z / L_{Ob})]^{-2/3}}{z^{-2/3}[1 - 7(z_r / L_{Ob})]^{-2/3}} \, . \qquad (48)$$

$C_T^2(z_r)$ is evaluated using the iterative technique described in section 4.2. Here, we again denote C_T^2 in the surface layer using C_{TS}^2. Knowing C_{TS}^2, equation 20 is used to evaluate C_n^2 for the surface layer. However, since a useful boundary layer equivalent of equation 29 does not exist due to the z-less stratification, we must postulate that C_{TS}^2 simply continues to the top of the layer:

$$X_X(z) = \log_{10}(C_{TS}^2) \, , \qquad (49)$$

where we use the quantity $X_X(z)$ to both distinguish from X_K, the daytime Kaimal vertical structure model in the boundary layer, and to establish that we are on largely unestablished ground. We know that the general behavior is diminishing C_n^2 with height. This will be accomplished with this functional form, primarily due to pressure and temperature decreases with height.

Combining this vertical form for C_T^2 with pressure and temperature vertical models, we produce an analog of equation 45:

$$N_X(z) = X_X(1000Z) + \log_{10}[A^2 P^2 / T^4] \, . \qquad (50)$$

In a similar fashion to equation 46, we thus produce a nighttime transition model to pass from the boundary layer constant C_T^2 assumption to the upper air CLEAR I night model. Since we have some confidence in this model, being based on measurements, we quickly transition to this model once out of the boundary layer. This accounts for the rather short transition distance parameter of $Z_i / 3$. Here, Z_i is the depth [km] of the total boundary layer from the surface to the base of the capping inversion.

$$N_N(Z) = \sigma\left(\frac{Z - 1.5Z_i}{Z_i / 3}\right) N_{mu}(Z) + \sigma\left(\frac{1.5Z_i - Z}{Z_i / 3}\right) N_X(Z) \, , \qquad (51)$$

where N_N is the total nocturnal log-base-10 C_n^2 model appropriate for ground level to 30 km. Based on variations that occur in C_n^2 levels in the surface layer coupled with comments from Beland, it is believed that this mean can be coupled with a log-standard deviation of approximately $\sigma = 0.5$ throughout the atmosphere under stable conditions.

8. Ground Level Point-to-Point Calculations

For ground level calculations we have the data as presented in figure 2 to guide us in determining how C_n^2 varies statistically along a single LOS. We also considered parameters ρ_0 and θ_0. The former, ρ_0 (equation 1), is directly proportional to r_0, the coherence diameter (Tofsted and Auvermann, 1991) which appears in both the long and short exposure optical transfer functions governing blur effects on passive optical systems (Goodman, 1985, section 8.7). However, in effects predictions models (including the Army's NVTherm) C_n^2 is currently treated as a constant of the propagation path. While this is seldom the case, our goal in this section is to express an effective C_n^2 value applicable for a specific path geometry. The influence of geometry is primarily in terms of the height of the LOS above the terrain, but also depends on the path weighting function associated with ρ_0. We further vary C_n^2 according to its temporal fluctuations.

The dependence on geometry may either be because target and observer are at different heights above the terrain (a slant path) or because the terrain is non-flat and therefore the ground falls away beneath the LOS. To simulate these changes we need a different form for ρ_0 than as expressed in equation 1. Rather than a slant path where s is a vertical parameter and φ represents the zenith angle, ground-to-ground paths require we invoke the equation (e.g., Beland, 1993; Tofsted and Auvermann, 1991),

$$\rho_0 = \left[1.46 k^2 \int_0^L C_n^2(z(s))(1 - s/L)^{5/3} ds \right]^{-3/5}, \qquad (52)$$

where s is now the distance along the path starting from the observer ($s = 0$) to the target ($s = L$), whereas previously s was a vertical distance. Further, C_n^2 is now a function of height above the surface (z) at each point along the path. We compare this calculation to a similar calculation where ρ_0 is computed using constant C_n^2. In this latter case C_n^2 can be passed through the integral sign and we obtain:

$$\rho_0 = \left[1.46 k^2 L C_n^2 \int_0^1 (1 - u)^{5/3} du \right]^{-3/5} = \left[1.46 k^2 L \frac{3}{8} C_n^2 \right]^{-3/5}. \qquad (53)$$

Our interest is in comparing the C_n^2 we should use to represent the path varying C_n^2 actually encountered. To do so, we will label the effective C_n^2 as $\overline{C_n^2}$. Associated with this turbulence

strength we have $\overline{\rho_0}$. For the effective C_n^2 ($\overline{C_n^2}$) to yield the same effect we simply equate $\rho_0 = \overline{\rho_0}$. Then, based on equations 47 and 48, upon canceling terms, we find,

$$\overline{C_{n\rho_0}^2} = \frac{1}{3/8}\int_0^1 C_n^2[z(uL)](1-u)^{5/3}\,du\,, \tag{54}$$

where $s = u_L$ permits us to non-dimensionalize the path integral.

As an example, we consider an LOS in which the terrain falls away beneath the optical path between an observer and target (effectively an overwatch situation). Let the observer's and target's initial heights be 2 m AGL. Assume the terrain drops away under the path as a quadratic function such that the center of the path is at 4.0 m AGL. From equation 13 we see that for even moderate height z the C_n^2 will behave almost with a height dependence of $z^{-4/3}$. We thus postulate this as a simple rule for this illustration: Let $C_n^2 = C_n^2(2)(z/2)^{-4/3}$. Then, assuming $C_n^2 = 5 \times 10^{-13}\,m^{-2/3}$ at 2 m height, upon integration we obtain an effective C_n^2 of $\sim 1.1 \times 10^{-13}\,m^{-2/3}$, a reduction almost a factor of 5, or by $\frac{2}{3}^{rds}$ of an order of magnitude. A reduction of this magnitude could significantly modify the computed effects of turbulence since a reduction of this order causes the ρ_0 parameter to increase by a factor of 2.5, which could be the difference between seeing and not seeing an object. Hence, somewhat trivial changes in terrain can have significant influences on the effective turbulence impacting a given LOS.

8.1   Numerical Evaluation

One significant question, however, is how to implement an LOS calculation such as equation 49. Obviously wargames pay a premium on LOS calculations and evaluating equation 49 for each intervisibility in the scenario comes at a significant cost.

To somewhat defray these costs, some shortcuts are possible. First, only those lines for which intervisibility occurs need be evaluated using equation 49. Second, the effects of equation 49 depend on the integrated C_n^2 over the entire path. Some coarseness in the evaluation is therefore acceptable. For example, the grain of the path integral need be no better than 100 m. Third, we can simplify the integral significantly if we store the C_n^2 height profile as an array of evenly spaced data points. Let δz be the interval between samples. Then, the index of the C_n^2 to use for each path segment is $i = z/\delta z$. Assuming constant C_n^2 within each path segment does not do great harm to the integration.

A further simplification involves discretizing the integral itself. Since the path will be determined from the intervisibility calculation, we could simply reuse the results of that calculation which should include range and height information. We first produce a table of results of the form

$$W_i = \frac{1}{3/8} \int_0^{x_i} (1-u)^{5/3} du \,, \tag{55}$$

where $x_i = i/1000$, and $i = 0...1000$. These results represent the integrated weighting value of the integrand in equation 49.

To use this W_i array, we need the total range from observer to target (L), a set of distances along this total path (s_k), and associated heights AGL (z_k). For each segment of the total path, we first compute the C_n^2 using the height z_k and the tabulated C_n^2 data (call this result K). We assume C_n^2 is constant over each path segment. Then, we compute the path position of the end of this segment, $z_k u_k = z_k s_k / L$. The appropriate index position in the W_i array is thus $i_k = 1000 u_k$. We then update a running sum which approximates the integral:

$$\overline{K} = \sum (W_{i_k} - W_{i_{k-1}})K_k \,. \tag{56}$$

8.2 Temporal Fluctuations

In addition to the mean effects of LOS height above the surface, for near-surface LOSs we need to consider temporal fluctuations. From figure 2, C_n^2 shows an approximately log-normal distribution. This data was obtained via a Lockheed scintillometer measuring integrated turbulence over a 950 m path, at 4 m AGL over roughly flat terrain. The data were collected over a 2-hour period around noon on a clear day (September 21, 2001) near the *Tank Tower*, an area of near-uniform desert creosote bush vegetation close to the southern border of WSMR, NM. Conditions were cloudless, and a review of temporal plots of wind and temperature indicated a statistically wide-sense stationary (e.g., Goodman, 1985) pattern of fluctuations. The C_n^2 appeared to only slightly increase in strength during the collection period. Recapping our description of the figure 2 data, the distribution was approximately log-normally distributed, with log-10-mean of -13.319 and log-10-standard deviation of 0.215. The turbulence outer scale for this path should be considerably shorter than 950 m such that paths of length greater than 950 m may be simulated assuming the path consists of $N = L/950$ independent identically-distributed segments of length 950 m each. The log-standard deviation of a path longer than 950 m should have a log-standard deviation reduced from its value over the 950 m path, such that $\sigma_L = 0.215/\sqrt{N}$. We can then generate a fluctuation of C_n^2 in log-10 space based on a weighted mean C_n^2 and a perturbation generated randomly based on σ_L. In this way we produce time varying path effects.

Again, however, we emphasize that this model applies to daytime atmospheric effects only. In the daytime surface layer the key conveyors of turbulent energy are vertically oriented convective plumes. The turbulence within such plumes is perhaps an order of magnitude stronger than the turbulence outside. For most paths we expect several such plumes of different turbulence strength to lie along a given path. As these plumes pass in and out of a given LOS they create fluctuations in the detected turbulence and result in characteristic autocorrelation

times of the turbulence. For the data presented in figure 2 this time constant is about 20 seconds, considerably shorter than the frame rate of any Army sensor. For a given glimpse along a given LOS, turbulence effects may thus be momentarily severe, but intervisibility conditions may be reestablished within a matter of seconds. If such effects are to be modeled in a wargame special attention should be given to ensure that the same perturbation statistic is used along a given LOS for both observer and target, even though the mean C_n^2 ($\overline{C_n^2}$) may be different. Also, the existence of a defeating level of turbulence along a given line may be only temporary and so should be updated approximately every 20 seconds with a new instantiation of the turbulent fluctuation.

For vertically oriented LOS's and slant paths the significant fluctuations in turbulence intensity appear to be concentrated in shear layers instead of vertically oriented plumes. To model such layers we will make a fluctuating vertical profile whose mean is determined by the combined upper layer associated with the CLEAR I night model and the KT profile. Between the top of boundary layer and the 10 km level associated with the start of the upper troposphere CLEAR I equation we will use a sigmoidal transitional function centered at 8 km with a width parameter of 2 km. We thus transition smoothly between the KT model and the CLEAR I model over roughly a 4 km interval.

9. Discussion

The structure of the nocturnal boundary layer environment has eluded researchers for perhaps the past 30 years. It is unlikely that we should do better than several more well funded efforts within a much shorter timeframe. This is not to say that we do not directly benefit from these prior developments. Indeed, significant work is available and has been used to gain a much more thorough understanding of this area than was available heretofore. However, much of it is conflicting and further time is necessary to sift the information into useful and redundant categories.

Significant information is available on nocturnal atmospheric processes of wind, temperature, and wave evolution as well as primarily empirical measured data. To integrate all this information has been difficult. In addition, we should point out that the daytime model proposed is useful for a noon timeframe only. Early morning and late afternoon conditions will tend to either evolve away from or reduce toward neutral condition profiles. Such profiles are not considered in the current effort. We expect to address these gaps in a future effort as well.

10. Conclusions

We have developed an initial picture of a vertical structure model of C_n^2 valid for a profile of atmospheric turbulence beginning at the surface and continuing through the upper troposphere. While not yet directly linked to meteorological conditions, it provides a characteristic sense of the strength of turbulence throughout an entire vertical column. Unlike previous models, it is integrated from the surface smoothly through each level, handling surface layer, mixed layer, and entrainment zone, and the troposphere to the tropopause for the daytime atmosphere. The time of applicability of the profile is nominally 12 noon currently, but is useful for calculations starting midmorning through midafternoon. Additional functionality will be considered in following developments. Currently, the user can select a value of C_n^2 at a specified reference altitude within the surface layer. A method is then specified for evaluating the Monin-Obukhov length to facilitate vertical scaling in the surface layer and its extension into the free convective layer. In the Executive Summary we have provided a concise recommendation regarding the specific equations to use to implement the technique discussed in this report.

References

Andrews, L.C.; Phillips, R.L. *Laser Beam Propagation through Random Media*, SPIE Press: Bellingham, WA, 1998.

Andrews, L.C.; Phillips R.L.; Hopen, C.Y. *Laser Beam Scintillation with Applications*, SPIE Press: Bellingham, WA, 2001.

Beland, R.R.; Brown, J.H.; Good, R.E.; Murphy, E.A. *Optical turbulence characterization of AMOS, 1985*; AFGL-TR-88-0153; Air Force Geophysics Laboratory, 1988.

Beland, R.R. *Propagation Through Atmospheric Optical Turbulence*, in *Atmospheric Propagation of Radiation*, Smith F.G., Ed.; The Infrared and Electro-Optical Systems Handbook, Vol. 2; SPIE Optical Engineering Press: Bellingham, WA, 1993.

Burk, S.D. Comparison of Structure Parameter Scaling Expressions with Turbulence Closure Model Predictions. *J. Atmos. Sci.* 1981, 38, 751–761.

Garvey, D. et al., *Atmospheric Characterization at the HIDL Site, CLEAR I Program, 29 August – 28 September 1984*, DR-85-0008; U.S. Army Atmospheric Sciences Laboratory: White Sands Missile Range, NM, 1985.

Goodman, J.W., *Statistical Optics*, J. Wiley & Sons, New York, 1985.

Hansen, F.V. *The Extrapolation of the Wind Profile with Height*, ASL Internal Report, Atmospheric Sciences Laboratory: White Sands Missile Range, NM, 1980.

Haugen, D.A., Ed.; *Workshop on Micrometeorology*, American Meteorological Society: Boston, MA, 1973.

Hoidale, M.M.; Newman, L. *Atmospheric Structure, White Sands Missile Range, New Mexico, Part 1, Surface Winds, Cloud Cover, Visibility*; DR-818; U.S. Army Electronics Command, Atmospheric Sciences Laboratory: White Sands Missile Range, NM, 1974.

Hoffert, M.I.; Storch, J. A Scheme for Computing Surface Fluxes from Mean Flow Observations. *Boundary-Layer Met.* 1979, 17, 429–442.

Hufnagel, R.E. *Propagation Through Atmospheric Turbulence*, Chap. 6, The Infrared Handbook, USGPO: Washington, D.C. 1974.

Kaimal, J.C.; Wyngaard, J.C.; Haugen, D.A.; Coté, O.R.; Izumi ,Y.; Caughey, S.J.; Readings, C.J. Turbulence Structures in the Convective Boundary Layer. *J. Atmos. Sci.* 1976, 33, 2152–2169.

Kaimal, J.C.; Finnegan, J.J. *Atmospheric Boundary Layer Flows, Their Structures and Measurement*, Oxford University Press: New York, NY, 1994.

Kukharets, V.P.; Tsvang, L.R. Structure parameter of the refractive index in the atmospheric boundary layer, *Izv. Atmos. Oceanic Phys.* 1980, 16, 73–77.

Kung, E.C. *Derivation of Roughness Parameter from Wind Profile Data above Tall Vegetation*, Studies of three dimensional structure of the planetary boundary layer; Annual Report; Department of Meteorology, University of Wisconsin, 1961.

Kung, E.C. *Climatology of Aerodynamic Roughness Parameter and Energy Dissipation in the Planetary Boundary Layer of the Northern Hemisphere*, Studies of the effects of variations in boundary conditions on the atmospheric boundary layer; Annual Report; Department of Meteorology, University of Wisconsin, 1963.

Kunkel, K.E., D.L. Walters, and G.A. Ely, *Behavior of the Temperature Structure Parameter in a Desert Basin*, *J. Appl. Met.* 1981, 20:130-136.

Kunkel, K.E.; Walters D.L. Modeling the Diurnal Dependence of the Optical Refractive Index Structure Parameter, *J. Geophys. Res.* 1983, 88, 10,999–11,004.

Kunkel, K.E.; Dowling, J.A.; Farmer, D.A. *HELSTF Atmospheric Turbulence Characterization*, Chap. 7, High Energy Laser Propagation Handbook, Vol. II: HEL System Test Facility Atmospheric Characterization; ASL-TR-0148; U.S. Army Atmospheric Sciences Laboratory, 1984.

MacArthur, C.D.; Haines, P.A. *The Roughness Lengths Associated with Regions of Heterogeneous Vegetation and Elevation*; ASL-CR-82-0206-1; Atmospheric Sciences Laboratory: White Sands Missile Range, NM, 1982.

Miller, M.G.; Zieske, P.L. *Turbulence Environmental Characterization*, RADC-TR-79-131, ADA072379; Rome Air Development Center, NY, 1979.

Moeng, C.H.; Wyngaard, J.C. Statistics of Conservative Scalars in the Convective Boundary Layer, *J. Atmos. Sci.*,1984, 41:3161–3169.

Nieuwstadt, F.T.M. Turbulence structure of the stable nocturnal boundary layer, *J. Atmos. Sci.* 1984, 41:2202–2216,.

Norton, C.; Hoidale, G. *The Diurnal Variation of Mixing Height by Month over White Sands Missile, NM*, ECOM-5579, U.S. Army Electronics Command, Atmospheric Sciences Laboratory: White Sands Missile Range, NM, 1975.

Paulson, C.A., "The Mathematical Representation of Wind Speed and Temperature Profiles in the Unstable Atmospheric Surface Layer," *J. Appl. Meteor.* 1970, 9:857–861.

Roggemann, M.C.; Welsh, B. *Imaging Through Turbulence*, CRC Press: Boca Raton, FL, 1996.

Tatarskii, V.I.; *Wave Propagation in a Turbulent Medium*, McGraw-Hill: New York, NY, 1961.

Stark, H.; Woods, J.W. *Probability, Random Processes, and Estimation Theory for Engineers*, Prentice-Hall: Englewood Cliffs, NJ, 1986.

Tofsted, D.H.; Auvermann, H.J. *Baseline Resolution of Atmosphere Related FADEWS Modeling Issues, Volume 9, Additional Model Improvements*; ASL-TR-0302; U.S. Army Atmospheric Sciences Laboratory: White Sands Missile Range, NM, 1991.

Ulrich, P.B. *Hufnagel-Valley profiles for specified values of the coherence length and isoplanatic angle;* MA-TN-88-013; W.J. Schafer Associates, 1988.

Valley, G.C., *Isoplanatic degradation of tilt correction and short-term imaging systems*, *Appl. Opt.* 1980, 19:574-577.

Wyngaard, J.C. *On Surface Layer Turbulence*, Chap 3, Haugen, D.A, Ed.; Workshop on Micrometeorology; American Meteorological Society: Boston, MA, 1973.

Abbreviations and Acronyms

AFG   Air Force Geophysics Laboratory

AGL   above ground level

AMOS   Air Force's Maui Optical Station

ASL   above sea level

CBL   convection boundary layer

CLEAR I   Critical Laser Enhancing Atmospheric Research I

HEL   high energy laser

HELHEM   High Engery Laser Handbook Empirical Model

H-V   Hufnagel-Valley

IR   infrared

LES   large eddy simulations

LOS   line-of-sight

MTF   modulation transfer function

NBL   nocturnal boundary layer

RHS   right hand side

rms   Root Mean Square

SBL   stable boundary layer

SLC   Submarine Laser Communication

UAV   Unmanned Aerial Vehicle

WSMR   White Sands Missile Range

Distribution List

No. of Copies	Organization

1 CD — US ARMY RESEARCH LAB
ATTN IMNE ALC IMS
MAIL & RECORDS MGMT
ADELPHI MD 20783-1197

1 ELEC — ADMNSTR
DEFNS TECHL INFO CTR
ATTN DTIC OCP V MADDOX
8725 JOHN J KINGMAN RD
STE 0944
FT BELVOIR VA 22060-6218

2 CDS — US ARMY RESEARCH LAB
AMSRD ARL CI OK TL
2800 POWDER MILL ROAD
ADELPHI MD 20783-1197

1 ELEC — US ARMY RESEARCH LAB
AMSRD CI OK TP TECHL LIB
APG MD 21005

1 CD — ARMY RESEARCH LABORATORY
ATTN AMSRD ARL D
2800 POWDER MILL ROAD
ADELPHI MD 20783-1197

1 CD — ARMY RESEARCH LABORATORY
ATTN AMSRD ARL RO EV
DR BACH
PO BOX 12211
RESEARCH TRIANGLE PARK, NC
27009

4 CDS — ARMY RESEARCH LABORATORY
ATTN AMSRD ARL CI EE
DR SHIRKEY
WSMR NM 88002-5501

1 CD — ARMY RESEARCH LABORATORY
ATTN AMSRD ARL CI EE
DR O'BRIEN
WSMR NM 88002-5501

4 CDS — ARMY RESEARCH LABORATORY
ATTN AMSRD ARL CI EE
D TOFSTED
WSMR NM 88002-5501

4 CDS — ARMY RESEARCH LABORATORY
ATTN AMSRD ARL CI EE
G VAUCHER
WSMR NM 88002-5501

1 CD — ARMY RESEARCH LABORATORY
ATTN AMSRD ARL CI CN
A TUNICK
ADELPHI MD 20783-1197

1 CD — ARMY RESEARCH LABORATORY
ATTN AMSRD ARL CI EE
D HOOCK
WSMR NM 88002-5501

1 CD — ARMY RESEARCH LABORATORY
ATTN AMSRD ARL SL BB
R SANDMEYER
APG MD 21005

1 CD — ARMY MATERIEL SYSTEMS
ANALYSIS ACTIVITY
ATTN AMXSY SC
J MAZZ
392 HOPKINS ROAD
APG MD 21005-5071

1 CD — ROBERT BELAND
AFRL/VSBY
29 RANDOLPH RD
HANSCOM AFB MA 01731-3010

1 CD — ARMY MODELING & SIMULATION
OFFICE
DA G37 DAMO-SBM
400 ARMY PENTAGON
WASHINGTON DC 20310-0450

1 CD   DIRECTOR USA TRADOC ANALYSIS
        CENTER
        ATTN ATRC WBC
        D DIXON
        WSMR NM 88002-5502

1 CD   US ARMY NIGHT VISION &
        ELECTRONIC SENSORS
        DIRECTORATE SENSOR
        PERFORMANCE MODELING BRANCH
        ATTN AMSRD CER NV MS
        E JACOBS
        10221 BURBECK ROAD
        FORT BELVOIR VA 22060-5806

1 CD   DIRECTED ENERGY DISTRIBUTED
        TEST CENTER
        ATTN SMDC RD TE H
        S EAST
        HELSTF
        WSMR NM 88002

1 CD   DIRECTOR USA TRADOC ANALYSIS
        CENTER
        ATTN ATRC WB
        P SHUGART
        WSMR NM 88002-5502

1 CD   DIRECTOR USA TRADOC ANALYSIS
        CENTER
        ATTN ATRC WA
        L SOUTHARD
        WSMR NM 88002-5502

1 CD   ERDC/CRREL
        ATTN DR G KOENIG
        72 LYME RD
        HANOVER NH 03755

1 CD   ARMY CORPS OF ENGINEERS
        TOPOGRAPHIC ENGINEERING
        CENTER
        DATA AND SIGNATURE ANALYSIS
        BRANCH
        FT BELVOIR VA 22060

1 CD   US MILITARY ACADEMY
        DEPT OF MATHEMATICAL SCIENCES
        THAYER HALL
        WEST POINT NY 10996-1786

2 CDS   UNITED STATES MILITARY
        ACADEMY
        COMBAT SIMULATION LABORATORY
        DR P WEST
        WEST POINT NY 10996

1 CD   USA PEO STRI
        FCS TRAINING IPT ENVIRONMENT
        D STEVENS
        12350 RESEARCH PKWY
        ORLANDO FL 32826-3276

1 CD   AFRL/IFOIL
        525 BROOKS ROAD
        ROME NY 13441-4505

1 CD   HQ USAFA/DFLIB
        2354 FAIRCHILD DRIVE SUITE 3A10
        USAF ACADEMY CO 80840-6214

1 CD   TECH CONNECT
        AFRL/XPTC
        BLDG 16, RM 107
        2275 D STREET
        WPAFB OH 45433-7226

1 CD   NAVAL RESEARCH LABORATORY
        MARINE METEOROLOGY DIVISION
        CODE 7543
        DR ANDY GOROCH
        7 GRACE HOPPER AVE
        MONTEREY CA 93943-5006

1 CD   US NAVAL WAR COLLEGE
        WAR GAMING DEPARTMENT CODE 33
        686 CUSHING ROAD
        NEWPORT RHODE ISLAND 02841-1207

1 CD   NAVAL POSTGRADUATE SCHOOL
        R K WOOD
        OR/WD
        1 UNIVERSITY CIRCLE
        MONTEREY CA 93943

1 CD   NAVAL POSTGRADUATE SCHOOL
        G SCHACHER
        DEPT OF PHYSICS
        1 UNIVERSITY CIRCLE
        MONTEREY CA 93943

1 CD   NAVAL POSTGRADUATE SCHOOL
        W B MAIER II
        DEPT OF PHYSICS
        1 UNIVERSITY CIRCLE
        MONTEREY CA 93943

1 CD   JWARS
        ATTN C BURDICK
        1555 WILSON BOULEVARD
        SUITE 619
        ARLINGTON VA 22209

1 CD   NORTHROP GRUMMAN
        INFORMATION TECHNOLOGY
        MELANIE GOUVEIA
        55 WALKERS BROOK DR.
        READING MA 01867

1 CD   NORTHROP GRUMMAN
        INFORMATION TECHNOLOGY
        DR HAIG ISKENDERIAN
        55 WALKERS BROOK DR.
        READING MA 01867

1 CD   NCAR LIBRARY SERIALS
        NATIONAL CENTER FOR
        ATMOSPHERIC RESEARCH
        PO BOX 3000
        BOULDER CO 80307-3000

1 CD   AFRL/VSBYA
        GEORGE Y JUMPER PHD PE
        29 RANDOLPH RD.
        HANSCOM AFB MA 01731-3010

TOTAL: 48 CDS AND 2 ELECTRONIC COPIES